STRUCTURAL BASIS FOR THE ACTIVATION OF RIG-I/MAVS

ANTIVIRAL IMMUNE SIGNALING

APPROVED BY SUPERVISORY COMMITTEE

Dr. Zhijian 'James' Chen

Dr. Qiu-Xing Jiang

Dr. Michael Rosen

Dr. Luke Rice

Dr. Qinghua Liu

DEDICATION

I would like to thank my mentors, Dr. Zhijian ‘James’ Chen and Dr. Qiu-Xing Jiang, for all the guidance and support. They are my role models showing me how to pursue science in endless enthusiasm. I really appreciate the comprehensive training I obtained from the two labs.

I would like to thank all the former and current members in our labs for their generous help and support. It is a great family of talented people. I would like to especially thank Dr. Lijun Josh Sun and Dr. Hui Zheng, who have been giving me tremendous guidance and help during my graduate study for my projects.

I appreciate the opportunity to have been working on these highly collaborative projects and learning from our talented collaborators. I would like to thank Dr. Kate Phelps and Abhijit Bugde in Live Cell Imaging Core Facility for guidance with cell imaging, Dr. Bryant Chhun at Carl Zeiss Microscopy, LLC for his technical expertise with SR-SIM imaging, Dr. Lily

Huang and Dr. Yue Ma in Department of Cell Biology for flow cytometry experiments, Ms Robyn Roth at Washington University at St Louis for freeze-etch EM study and Dr. Xu Zhang and Structural Biology Core Facility for guidance with crystallization. I would like to especially thank Dr. Xuewu Zhang and Dr. Xiaojing He in Department of Pharmacology for our close collaboration and discussion on the MAVS project, Dr. Zhiheng Yu and Michael Jason de la Cruz at HHMI Janelia Farm Research Campus for their help with cryoEM data collection and cryoET experiments. I am extremely grateful to Dr. Z. Hong Zhou, Dr. Peng Ge and Ke Ding at UCLA for their tremendous guidance and help on EM data analysis.

I would like to thank my thesis committee, Dr. Michael Rosen, Dr. Luke Rice and Dr. Qinghua Liu, not only for their insightful suggestions on my projects, but also tremendous support and encouragement.

Finally, I would like to especially thank my parents and my husband, who have been my strongest support during these years.

STRUCTURAL BASIS FOR THE ACTIVATION OF RIG-I/MAVS ANTIVIRAL IMMUNE SIGNALING

by

HUI XU

DISSERTATION

Presented to the Faculty of the Graduate School of Biomedical Sciences

The University of Texas Southwestern Medical Center at Dallas

In Partial Fulfillment of the Requirements

For the Degree of

DOCTOR OF PHILOSOPHY

The University of Texas Southwestern Medical Center at Dallas

Dallas, Texas

May, 2015

STRUCTURAL BASIS FOR THE ACTIVATION OF RIG-I/MAVS ANTIVIRAL IMMUNE SIGNALING

Publication No. _____

HUI XU, Ph.D

The University of Texas Southwestern Medical Center at Dallas, 2015

Supervising Professors: Dr. Zhijian 'James' Chen
Dr. Qiu-Xing Jiang

Retinoic acid inducible gene-I (RIG-I) is a key cytosolic pathogen RNA sensor that activates mitochondrial antiviral signaling protein (MAVS) to trigger rapid innate immune responses. Using RNAs of different lengths as model ligands, we showed that RIG-I oligomerized on dsRNA in an ATP hydrolysis-dependent and dsRNA length-dependent manner, which correlated with the strength of type-I interferon (IFN-I) activation. The obtained negative stain EM structure of full-length RIG-I in complex with a 5'ppp stem-loop RNA and the crystal structure of RIG-I/Ub complex elucidated a two-step oligomerization and conformational change of RIG-I for activation. RIG-I oligomers nucleate MAVS through

homotypic interaction of the N-terminal caspase activation and recruitment domains (CARDs) and induce the formation of prion-like aggregates. The obtained cryoEM structure of left-handed helical filaments of MAVS CARD revealed specific interfaces between individual CARD subunits that are dictated by a combination of electrostatic and hydrophobic interactions and hydrogen bonding. Point mutations at multiple locations of these interfaces impaired filament formation and antiviral signaling. Super-resolution imaging of virus-infected cells revealed rod-shaped MAVS clusters on mitochondria. These results elucidated the structural mechanism of RIG-I activation by RNA and K63-linked ubiquitin chains as well as the activation of MAVS through polymerization, revealing a highly efficient signaling cascade for viral RNA sensing.

TABLE OF CONTENTS

PRIOR PUBLICATIONS

Xu, H., He, X., Zheng, H., Huang, L. J., Hou, F., Yu, Z., de la Cruz, M. J., Borkowski, B., Zhang, X., Chen, Z. J., Jiang, Q. X. (2014). Structural basis for the prion-like MAVS filaments in antiviral innate immunity. ***eLife*** 3, e01489.

Peisley, A., Wu, B., **Xu, H.,** Chen, Z. J., Hur, S. (2014). Structural basis for ubiquitin-mediated antiviral signal activation by RIG-I. ***Nature*** 509, 110-114.

Cai, X., Chen, J., **Xu, H.,** Liu, S., Jiang, Q. X., Halfmann, R., Chen, Z.J. (2014). Prion-like polymerization underlies signal transduction in antiviral immune defense and inflammasome activation. ***Cell*** 156, 1207-1222.

Zhang, X., Wu, J., Du, F., **Xu, H.,** Sun, L., Chen, Z., Brautigam, C. A., Zhang, X., and Chen, Z. J. (2014). The cytosolic DNA sensor cGAS forms an oligomeric complex with DNA and undergoes switch-like conformational changes in the activation loop. ***Cell reports*** 6, 421-430.

Llaguno, M. C., **Xu, H.,** Shi, L., Huang, N., Zhang, H., Liu, Q., and Jiang, Q. X. (2014). Chemically functionalized carbon films for single molecule imaging. ***Journal of structural biology*** 185, 405-417.

LIST OF FIGURES

LIST OF TABLES

LIST OF SUPPLEMENTAL FILES

MOVIE 1

CHAPTER ONE
INTRODUCTION

Pattern recognition receptors (PRRs) in innate immunity

Viral infection of host cells triggers innate and adaptive immune responses that are essential for the survival of the host (Iwasaki and Medzhitov, 2010; Ronald and Beutler, 2010; Takeuchi and Akira, 2010). The innate immune system serves as the first line of defense against viral infection. It not only mounts a rapid antiviral response within hours of infection, but also ultimately helps initiate the adaptive immune system. Initiation of innate immune response relies on a group of pattern recognition receptors (PRRs), which recognize distinct evolutionarily conserved molecular structures known as pathogen-associated molecular patterns (PAMPs). PAMPs, such as pathogen-derived nucleic acids, lipopolysaccharide (LPS), peptidoglycan and flagellin, are characterized by being invariant among pathogens of a given class, essential for the survival of the pathogen, and distinguishable from 'self' (Mogensen, 2009). Two groups of pattern recognition receptors are responsible for detecting viral RNAs. The first group is a family of transmembrane proteins called Toll-like receptors (TLRs), located on the cell surface or in endosomal membranes and acting as sensors of viral RNAs encountered in extracellular environment (Kawai and Akira, 2006). The second group of sensors resides in the cytosol. They belong to a family of cytosolic RNA helicases called RIG-I-like receptors (RLRs), including retinoic acid inducible gene-I (RIG-I), melanoma differentiation-association gene 5 (MDA5) and laboratory of genetics and physiology 2 (LGP2) (Yoneyama and Fujita, 2009). Unlike TLRs,

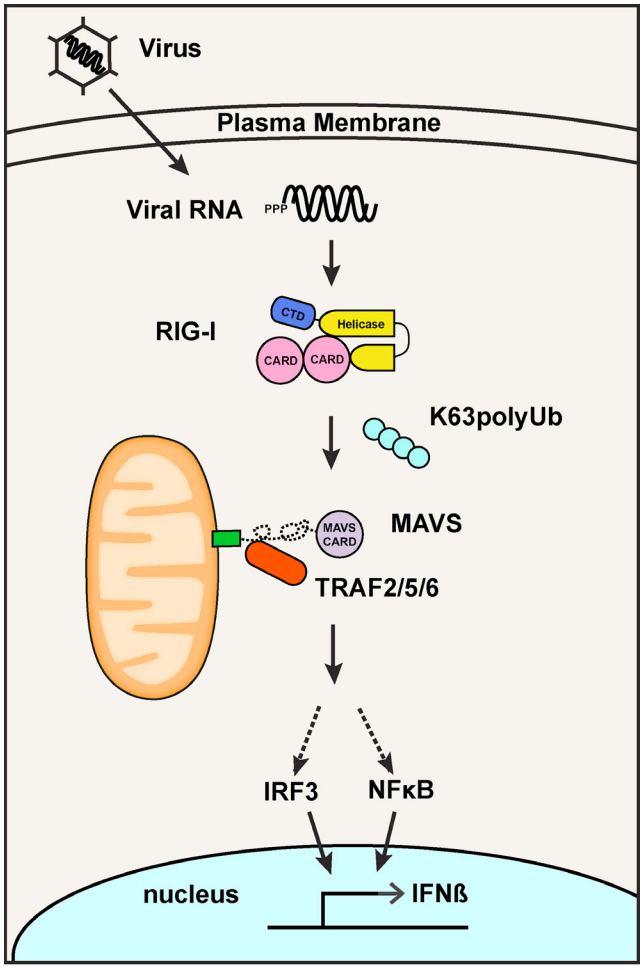

Figure 1 The RIG-I/MAVS Antiviral Pathway
Upon virus infection, viral RNA in the cytoplasm is detected by RIG-I-like receptors (RLRs), which undergo a conformational change and interact with unanchored K63-linked polyubiquitin chains. The binding to dsRNA and polyubiquitin drives RLRs to form active oligomers, which then activate MAVS, an adaptor protein localized on the mitochondrial outer membrane. Active form of MAVS in turn recruits E3 ligases TRAF proteins to activate downstream kinases IKK and TBK1, which subsequently lead to the activation of two transcription factors NF-κB and IRF3, respectively. IRF3 dimer and NF-κB heterodimer translocate to nucleus where they coordinately induce the production of type-I interferon and inflammatory cytokines.

which are mainly expressed in immune cells, such as macrophages and dendritic cells, RIG-I-like receptors are ubiquitously expressed in immune and non-immune cells, including fibroblasts, epithelial cells and endothelial cells. Recognition of viral RNAs by RLRs leads to

the activation of mitochondrial antiviral signaling protein (MAVS; also known as IPS1, VISA and CARDIF). Activated MAVS triggers rapid production of type-I interferon and proinflammatory cytokines (Figure 1; Kawai et al., 2005; Meylan et al., 2005; Seth et al., 2005; Xu et al., 2005).

RIG-I-like receptors (RLRs)

As the founding member of the RIG-I-like receptors (RLRs), RIG-I was first reported as a retinoic acid-inducible gene in 1997 (GenBank: AF038963) and later identified as a DExD/H-box-containing protein required for intracellular dsRNA-induced IFN production (Yoneyama et al. 2004). RIG-I and MDA5 are two DExD/H-box helicases that belong to the superfamily 2 of RNA helicases (Yoneyama et al., 2004; Fairman-Williams et al., 2010). Both proteins are large, multidomain proteins that are highly conserved among vertebrates. Both RIG-I and MDA5 contain N-terminal tandem caspase activation and recruitment domains (CARDs), a central RNA helicase, and a C-terminal regulatory domain (CTD) (Figure 2A). The CARDs, which are small helical bundles of the death-domain superfamily, are responsible for transmitting the activation signal downstream. The helicase domain has an active site for ATP binding and hydrolysis, as well as jointly forming an extended RNA-binding surface with the CTD. The CTD binds to the RNA ligands and confers part of the ligand specificity. In contrast, the third member of the RLRs, LGP2, lacks CARD domains and instead serves as an important regulator in the RIG-I and MDA5 pathways. It is still controversial whether it promotes or inhibits the RLR signaling pathway (Yoneyama et al., 2005; Venkataraman et al., 2007; Satoh et al., 2010).

Ligands for RLRs

Despite sharing a similar domain structure, RIG-I and MDA5 recognize viral RNA ligands through distinct mechanisms (Kato et al., 2008; Loo et al., 2008; Iwasaki, 2012). RIG-I preferentially binds to short blunt-ended base-paired RNA with a 5' triphosphate cap (denoted 5'pppbpRNA, since it could arise from ssRNA with complementary ends or dsRNA) (Hornung et al., 2006; Schlee et al., 2009; Kolakofsky et al., 2012). 5'ppp modification is a distinct feature of pathogen RNAs that distinguishes nonself and self RNAs. RIG-I CTD specifically recognizes the 5'ppp modified blunt end of RNA with significantly higher affinity and longer off-rate compared with 5'ppp ssRNAs, 5'OH bpRNAs or RNAs with 5' or 3' overhangs (Lu et al., 2010; Wang et al., 2010; Jiang et al., 2011). Besides the lower intrinsic binding affinity of RIG-I to 5'OH bpRNAs, it has also been reported that much longer dsRNAs (>200 bp), including poly(I:C), can also induce IFN via RIG-I (Strahle et al., 2007; Kato et al., 2008; Binder et al., 2011). This could be related to the ability of RIG-I to translocate along dsRNA (Myong et al., 2009) or the need for RNA-mediated RIG-I multimerization to promote interaction with MAVS (see below). In addition, 5′-hydroxyl (5′-OH) and 3′-monophosphoryl short RNA molecules with double-stranded stems generated by RNase L have also been reported as RIG-I ligands (Malathi et al., 2007; Malathi et al., 2010). In order to study the physiological agonists for RIG-I in virus-infected cells, one study isolated RIG-I-bound RNA after viral infection and used next-generation RNA sequencing to show that RIG-I preferentially associates with short 5′ppp-containing viral RNA segments in cells infected with influenza and Sendai viruses (Baum et al., 2010). RIG-I may react to

different forms of RNA upon simulation depending on different cell types under different circumstances.

In contrast to RIG-I, MDA5 preferentially binds internally to long dsRNA (>1,000bp) with no end specificity (Kato et al., 2008). As a result, RIG-I and MDA are able to combat against a large variety of viruses. RIG-I can be activated by viruses in the Paramyxoviridae family, such as Sendai virus (SeV) and Newcastle disease virus (NDV); viruses in the Flaviviridae family, such as Hepatitis C virus (HCV); and viruses in the Rhabdoviridae family, such as vesicular stomatitis virus (VSV). MDA5 detects viruses in the Picornaviridae family, such as Polio virus and Encephalomyocarditis virus (EMCV). Some viruses, including West Nile virus (WNV), Reovirus and Dengue virus are recognized by both RIG-I and MDA5 (Kato et al., 2006; Loo et al., 2008; Loo and Gale, 2011; Wu and Chen, 2014).

Structural basis of RLR activation upon RNA binding

Despite the obvious need for structural information on RIG-I to understand its activation mechanism, for a long time the protein remained intractable to crystallization. Finally, in a short period of time in 2011, four groups independently reported crystal structures of different domains of RIG-I and in complexes with RNAs (Table 1). Despite differences due to species, presence or absence of nucleotide, and RNA length and sequence, all structures give a consistent picture of the domain arrangement of RIG-I and how RIG-I binds to bpRNA.

In the absence of dsRNA ligand, RIG-I is in an autoinhibited state. The helicase domain, composed of two Rec A domains (Hel-1 and Hel-2; the SF2 helicase core) and a

Table 1 RIG-I crystal structures

	Structure	PDB	Paper
RNA bound	dRIG-I Helicase (residues 242-794) + 19mer 5'OH blunt-ended dsRNA + ADP-AlF_3 (transition-state analog)	4A36	Kowalinski et al., 2011
	dRIG-I CTD (residues 806-933) +14mer 5'OH blunt-ended dsRNA	4A2X	
	hRIG-I Helicase+CTD (residues 230-925) + 10mer 5'OH blunt-ended dsRNA no nucleotide	2YKG	Luo et al., 2011
	hRIG-I Helicase+CTD (residues 232-925) + 14mer 5'OH blunt-ended dsRNA + ADP-BeF_3 (transition-state analog)	3TMI	Jiang et al., 2011
	hRIG-I Helicase+CTD (residues 239-925) + 8bp 5'ppp stem-loop RNA + ADP	4AY2	Luo et al., 2012
RNA free	dRIG-I full-length (residues 1-933)	4A2W	Kowalinski et al., 2011
	dRIG-IΔCTD(residues 1-794)	4A2Q	
	dRIG-I Helicase (residues 242-794)	4A2P	
	dRIG-I CTD (residues 806-933)	4A2V	
	mRIG-I Helicase + AMP-PNP	3TBK	Civril et al., 2011

family-specific large insertion within Hel-2 (referred to as Hel-2i), is in an open conformation (Figure 2B). Whereas Hel2 and Hel2i form a rigid unit, the position of Hel1 in the various structures has a large angular distribution due to the flexibility of the two inter-domain connections (Kowalinski et al. 2011). So far the only crystal structures that include the CARDs are ligand-free dRIG-I constructs (Kowalinski et al. 2011). The tandem CARDs form a rigid, head-to-tail unit. CARD1 is largely solvent exposed and its C-terminus links directly to the extended N-terminal helix of CARD2. The other end of CARD2 binds to the Hel2i domain via a substantial interface. This conformation sterically prevents the CARDs from binding to polyubiquitin, thereby preventing signaling to MAVS (see below). There is a unique, elbow-shaped helical extension, denoted as the bridging helices (Br, Fig 2A;

Kowalinski et al. 2011) or pincer domain (Luo et al. 2011) that connect Hel-2 to CTD. The CTD is not visible in the electron density of the full-length RIG-I crystals, although gel analysis of dissolved crystals shows the RIG-I to be intact. This suggests that the CTD is flexibly linked to the end of the bridging helices (Figure 2B), consistent with the absence of significant interaction between the isolated CTD and the other domains of RIG-I *in vitro* (Kowalinski et al. 2011). This intrinsic inter- and intra-domain flexibility of RIG-I may contribute to the difficulty in obtaining a crystal structure of the full-length protein in RNA free or bound form.

In the presence of a viral dsRNA, RIG-I undergoes significant conformational rearrangement (Figure 2C). The CTD binds tightly to the blunt end of RNA and the helicase domains wrap around the RNA, adopting a disk shape (approximate diameter 75 Å, length 45 Å). The central, negatively charged cavity (approximate diameter 25 Å, length 30 Å) accommodates ~9 bp of dsRNA. The CTD of RIG-I specifically interacts with 5'ppp, while the helicase domain, predominantly the Hel2i domain, interacts with the phosphate sugar backbone of dsRNA through non-specific interactions (Figure 2D). This conformational change allows ATP to bind RIG-I, a necessary step for the activation of RIG-I (Kowalinski et al., 2011; Luo et al., 2011; Jiang et al., 2011; Luo et al., 2012). Although the CARDs were absent from the RNA-bound RIG-I crystal structures, biochemical studies and small angle X-ray scattering data indicate that the tandem CARDs are released from the Hel2i domain in the active form of RIG-I (Figure 2C; Luo et al., 2011; Jiang et al., 2011).

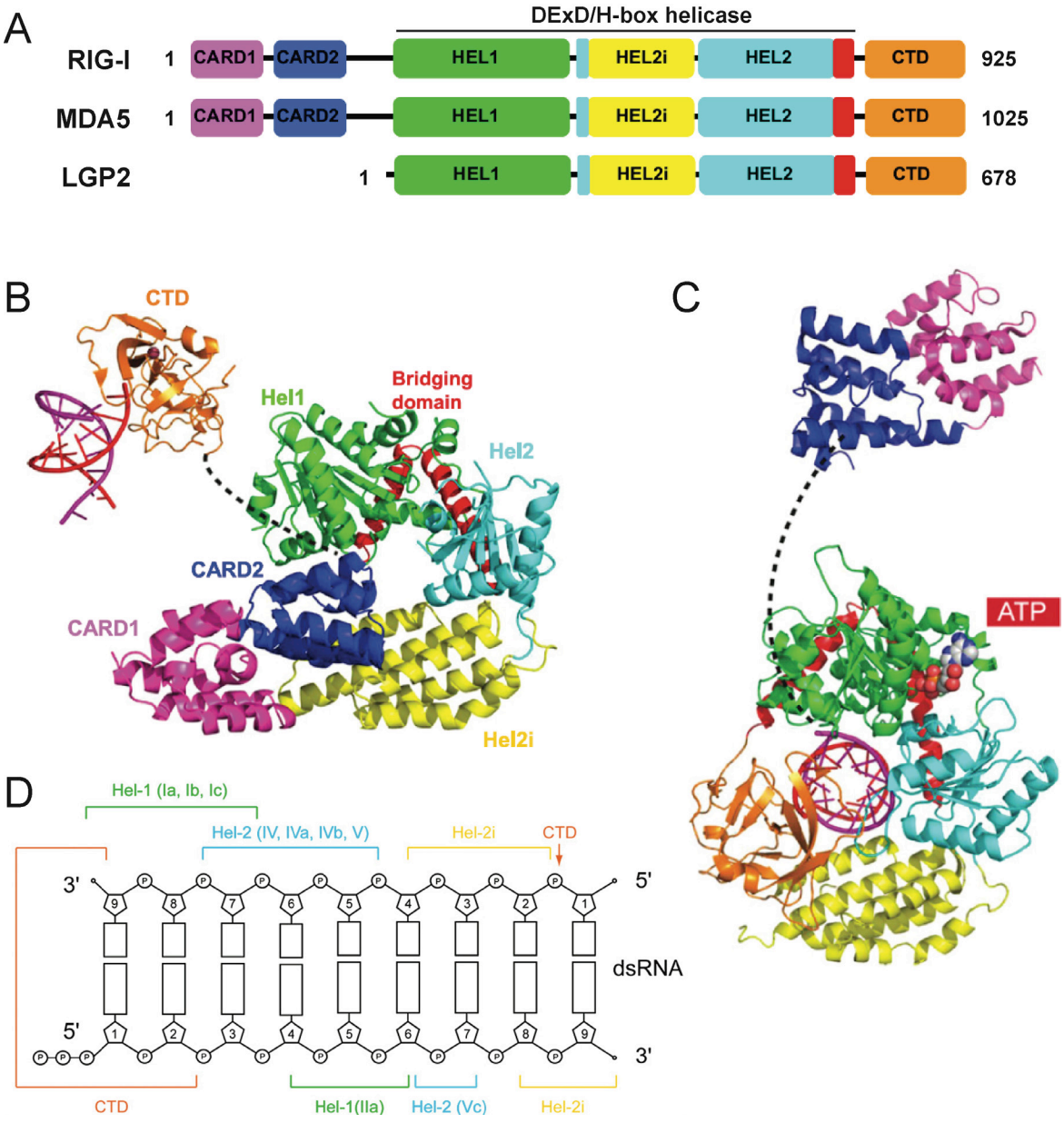

Figure 2 Conformational changes associated with activation of RIG-I. (Adapted from Kolakofsky et al., 2012)

(A) A color-coded schematic representation of domain structures of RIG-I, MDA5 and LGP2. Bare lines represent flexible linkers.

(B) Model of the autoinhibited state of duck RIG-I (PDB: 4A2W). The flexibly linked CTD (invisible in the crystal structure) has been included to illustrate that it is free to detect and bind 5'ppp bpRNA as the first step in activation. The CARDs, bound to Hel-2i via CARD2, are unavailable for signaling in this form.

(C) Model of the activated state of human RIG-I (PDB: 3TMI) with added CARDs on a 55-residue long flexible linker. In B and C, the Hel-2i domains (yellow) are superposed to show

that CARD2 binding to Hel-2i is incompatible with the bound position of the dsRNA and CTD.
(D) Schematic diagram of contacts of various domains and motifs of human RIG-I to dsRNA based on Jiang et al. (2011) and Kowalinski et al. (2011).

The ATPase activity of RIG-I is required for its activation (Yoneyama et al., 2004). In the ATP-analog-bound forms of the complex, domains of RIG-I (Hel1, Hel2, Hel2i, CTD) make complementary contributions to the elaborate network of mainly polar interactions with both strands of the dsRNA (Figures 3C and D). In the nucleotide-free and ADP-bound complexes (Luo et al., 2011, 2012), the helicase is in an open state (Figures 3A and B) with the disordered Hel-2 not contributing to RNA binding and Hel2i making different contacts due to its slightly rotated position. Upon ATP hydrolysis, RIG-I displays ATP-dependent translocation along bpRNA (Myong et al., 2009). This may bring multiple copies of RIG-I in close proximity on the dsRNA depending on the length of RNA (Peisley et al., 2013).

A recent crystal structure of the MDA5 helicase domains and CTD bound to dsRNA revealed how MDA5, despite having a similar domain architecture as RIG-I, recognizes dsRNA in a different manner (Wu et al., 2013). Unlike RIG-I, MDA5 is not preferentially activated by 5′ppp dsRNA (Kato et al., 2006, 2008). Although the helicase domains of MDA5 wrap around dsRNA similarly to the helicase domains of RIG-I, the MDA5 CTD is rotated by 20°, bringing it closer to the dsRNA, as compared to the RIG-I structure (Peisley et al., 2013; Wu et al., 2013; Reikine et al., 2014). The CTD also forms contact with Hel1 in MDA5, such that MDA5 forms a closed ring around the dsRNA (Figure 3E; Wu et al., 2013). This promotes cooperative filament formation along dsRNA, initiated from internal sites in the dsRNA rather than from one of the ends, and leaves the tandem CARDs of MDA5

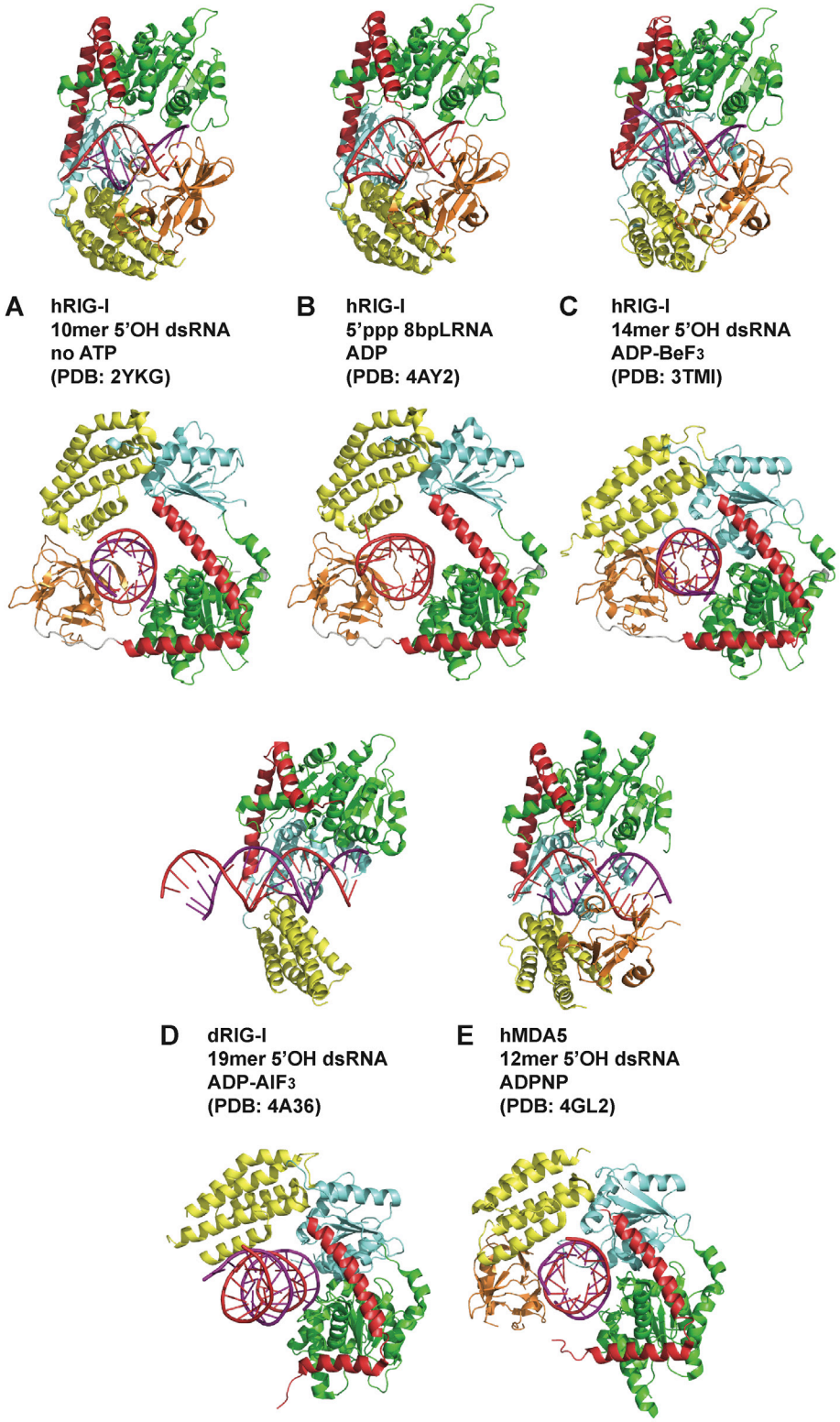

Figure 3 Crystal structures of RIG-I or MDA5 bound to RNA.

(A) Human RIG-IΔCARDs with a 10mer dsRNA but no nucleotide at 2.5 Å resolution (PDB: 2YKG) (Luo et al., 2011).
(B) Human RIG-IΔCARDs in complex with a 5'ppp 8bp stem-loop RNA and ADP at 2.8Å resolution (PDB: 4AY2) (Luo et al., 2012).
(C) Human RIG-IΔCARDs in complex with a 14mer dsRNA and the transition-state analog ADP-BeF_3 at 2.9 Å resolution (PDB: 3TMI) (Jiang et al., 2011).
(D) Duck RIG-IΔCARDsΔCTD in complex with a 19mer dsRNA and the transition-state analog ADP-AlF_3 at 3.7 Å resolution (PDB: 4A36) (Kowalinski et al., 2011).
(E) Human MDA5ΔCARDs (residues 298-644, 663-1017) in complex with a 12mer dsRNA and the ATP analog ADPNP at 3.56Å resolution (PDB: 4GL2) (Wu et al., 2012).

flexibly exposed on the periphery of the filament (Peisley et al., 2011; Berke et al., 2012). ATP hydrolysis causes MDA5 to dissociate from the dsRNA, contributing to the dynamics of MDA5 filament assembly and disassembly (Peisley et al., 2011; Berke et al., 2012).

Role of unanchored lysine 63-linked ubiquitin chains in RLR activation

The conformational changes of RIG-I and MDA5 upon RNA binding release the N-terminal tandem CARDs from the autoinhibited state (Figures 2B and C), but this is not sufficient for the full activation. *In vitro* reconstitution of RIG-I signaling revealed that in addition to activation by RNA, the binding of unanchored K63 polyubiquitin to the exposed RIG-I CARDs is essential for a full signaling response as measured by IRF3 dimerization (Zeng et al., 2010). Polyubiquitin chains containing as few as two ubiquitin molecules bind non-covalently to the RIG-I CARDs and can also be covalently attached to RIG-I by the E3 ligase TRIM25 (Zeng et al., 2010; Gack et al., 2007). In the presence of RNA and ATP, the binding to K63 polyubiquitin induced RIG-I to form active tetramers (Jiang et al., 2012). The latter gain a high capacity of activating MAVS on mitochondria, presumably through CARD-CARD interactions. Similar studies generalized these findings to MDA5 and showed that the

oligomerization of MDA5 CARDs by K63 polyubiquitins is essential for the activation of the pathway in cells (Zeng et al., 2010; Jiang et al., 2012).

Mechanism of MAVS activation

MAVS is ubiquitously expressed and localized to the mitochondrial outer membrane. It consists of an N-terminal CARD domain, a proline-rich region (PRR) preceding a poorly structured middle segment, and a C-terminal monotopic transmembrane (TM) domain (Figure 7A). Recent studies have shown that upon activation, MAVS molecules polymerize themselves into large functional aggregates (Hou et al., 2011). These high molecular weight aggregates behave like prion fibers, because they are detergent-resistant, protease-resistant and self-perpetuating by inducing inactive MAVS to form functional aggregates. Cell free assays revealed that the CARD domain of MAVS (which lacks the signaling domain) is essential and sufficient to convert endogenous full-length MAVS into SDS-resistant polymers that are functional in triggering downstream signaling (Hou et al., 2011). Subsequent study showed that MAVS CARD indeed functions like a *bona fide* prion in yeast (Cai et al., 2014).

The CARD domain of MAVS shares some homology with the first CARD domains in both RIG-I and MDA5 (20% and 25% sequence identity respectively). The crystal structure of MAVS CARD, fused to maltose-binding protein (MBP), exhibits a typical helical bundle of six antiparallel α-helices (Potter et al., 2008). However, unlike the CARD domains of RIG-I or MDA5, the isolated MAVS CARD without MBP self-assembles into filamentous

structures (Hou et al., 2011). How the CARD domain triggers the formation of functional MAVS aggregates remains to be addressed.

Signaling downstream of MAVS

Recently, studies in our lab showed that the activated MAVS polymers recruit multiple E3 ligases, TRAF proteins, including TRAF2, TRAF5, and TRAF6, through distinct TRAF-binding motifs (Liu et al., 2013). TRAF2 and TRAF5 act redundantly with TRAF6 to promote ubiquitination reactions that recruit NEMO to the MAVS signaling complex, which then turns on two cytosolic protein kinases IKK and TBK1, leading to the activation of transcription factors NF-κB and IRF3, respectively (Figure 1; Liu et al., 2013). Activated NF-κB and IRF3 are translocated into the nucleus, where they induce expression of type-I interferon and other inflammatory cytokines.

In my thesis project, I focused on understanding the structural basis of the activation of RIG-I/MAVS antiviral immune signaling. Despite the significant insights of RIG-I domain rearrangement upon RNA binding revealed by several crystal structures, it was not clear why the ATPase activity of RIG-I is essential for its activation. Using *in vitro*-transcribed RNAs of different lengths as model ligands, I showed that RIG-I oligomerized on 5'ppp dsRNA in an ATP hydrolysis-dependent and dsRNA length-dependent manner, which correlated with the strength of type-I interferon (IFN-I) activation. To study the domain rearrangement of full-length RIG-I upon RNA binding, I obtained the negative stain EM structure of full-length RIG-I in complex with a 5'ppp stem-loop RNA and ATP. I synthesized and purified K63-linked polyubiquitin chains and in collaboration with Dr. Sun Hur lab at Harvard

University, solved the crystal structure of RIG-I/Ub complex. These structures suggested a two-step oligomerization of RIG-I: dsRNA mediated 'beads on the string' oligomerization and K63polyUb binding induced oligomerization of RIG-I CARDs.

To understand the structural basis underlying MAVS polymerization, we obtained the cryoEM reconstruction of MAVS CARD filaments at 4.25 Å resolution. Based on the cryoEM map and the crystal structure of the individual MAVS CARD, I built a pseudoatomic model of the filament and identified three CARD-CARD interfaces that are important for filament formation. Mutations of residues at these interfaces disrupted MAVS self-association and abrogated the activation of the signaling pathway in cells. Another cryoEM reconstruction of MAVS CARD filaments with a different symmetry was obtained earlier and compared here. In order to understand the domain arrangement of the native MAVS aggregates, I also collected cryoEM images of a nearly full-length MAVS protein without part of the proline-rich region (PRR) and the C-terminal transmembrane domain (MAVSΔProTM). MAVSΔProTM formed thicker filaments displaying similar helical symmetry with MAVS CARD filaments. These structural studies showed that MAVS CARD filament forms the core of MAVS aggregates, suggesting a novel mechanism to expose the central segments of MAVS for downstream signaling effector recognition and signal amplification. To visualize the full-length MAVS filaments in virus-infected cells, I obtained three-dimensional Structured Illumination Microscopic (3D-SIM) images that achieved a sufficiently high resolution for us to discern the rod-shaped MAVS clusters on the mitochondria, providing evidence for MAVS fiber formation in cells. In accordance with the cryoEM studies, point mutations that disrupted MAVS filament formation abrogated the

redistribution and aggregation of MAVS on mitochondrial membrane and blocked the induction of interferon-β (IFNβ) in response to RNA virus infection. To study the activation of full-length MAVS *in vitro*, I devised a protocol to purify functional full-length MAVS in the inactive state from uninfected HEK293T cells stably expressing Flag-MAVS. The purified protein gained activity by interacting with MAVS CARD filaments, which further suggested that MAVS activation occurred through a prion-like mechanism triggered and templated by the N-terminal CARD domain. These results elucidated the structural mechanism for the formation of functional MAVS filaments.

CHAPTER TWO
RESULTS

ATP hydrolysis triggered RIG-I oilgomerization upon RNA binding

ATP hydrolysis by RIG-I after binding to RNA is critical for downstream activation (Yoneyama et al., 2004). The exact function of the ATPase activity of RIG-I was not clear until it was reported that after binding to the 5'ppp end of dsRNA, RIG-I is capable of translocating on dsRNA in an ATP hydrolysis-dependent manner (Myong et al., 2009). To dissect the role of RNA binding, ATP hydrolysis and ATP-dependent translocation of RIG-I on dsRNA, a variety of RNAs were tested for their biochemical and biophysical features of RIG-I binding and activity. Since RIG-I binding occupies 9-10bp RNA, I used dsRNAs of 17, 19, 22 or 35bp in length which can theoretically accommodate 1, 2 or 3 RIG-I molecules. In addition to dsRNAs, which have two ends available for RIG-I binding, a 51mer RNA with predicted stem-loop structure was also tested (22bp 5'ppp bpLRNA, Figure 4A). It has a 7nt loop and a 22bp stem that is long enough to accommodate two RIG-I molecules as predicted by the crystal structures of RNA bound form of RIG-IΔCARD (Jiang et al., 2011; Luo et al., 2011, 2012). 5'ppp RNAs were generated by *in vitro* transcription by T7 RNA polymerase followed by gel purification. The complex formed by RIG-I and RNA was detected by native gel electrophoresis followed by Coomassie Blue staining of RIG-I or Ethidium Bromide (EB) staining of RNA. In the absence of ATP, RIG-I bound to the end of 22bp 5'ppp bpLRNA or two ends of dsRNAs, forming a monomeric or dimeric complex (Figure 4B). In the presence of ATP, in addition to the minimal RNA-binding unit of RIG-I, bands corresponding to

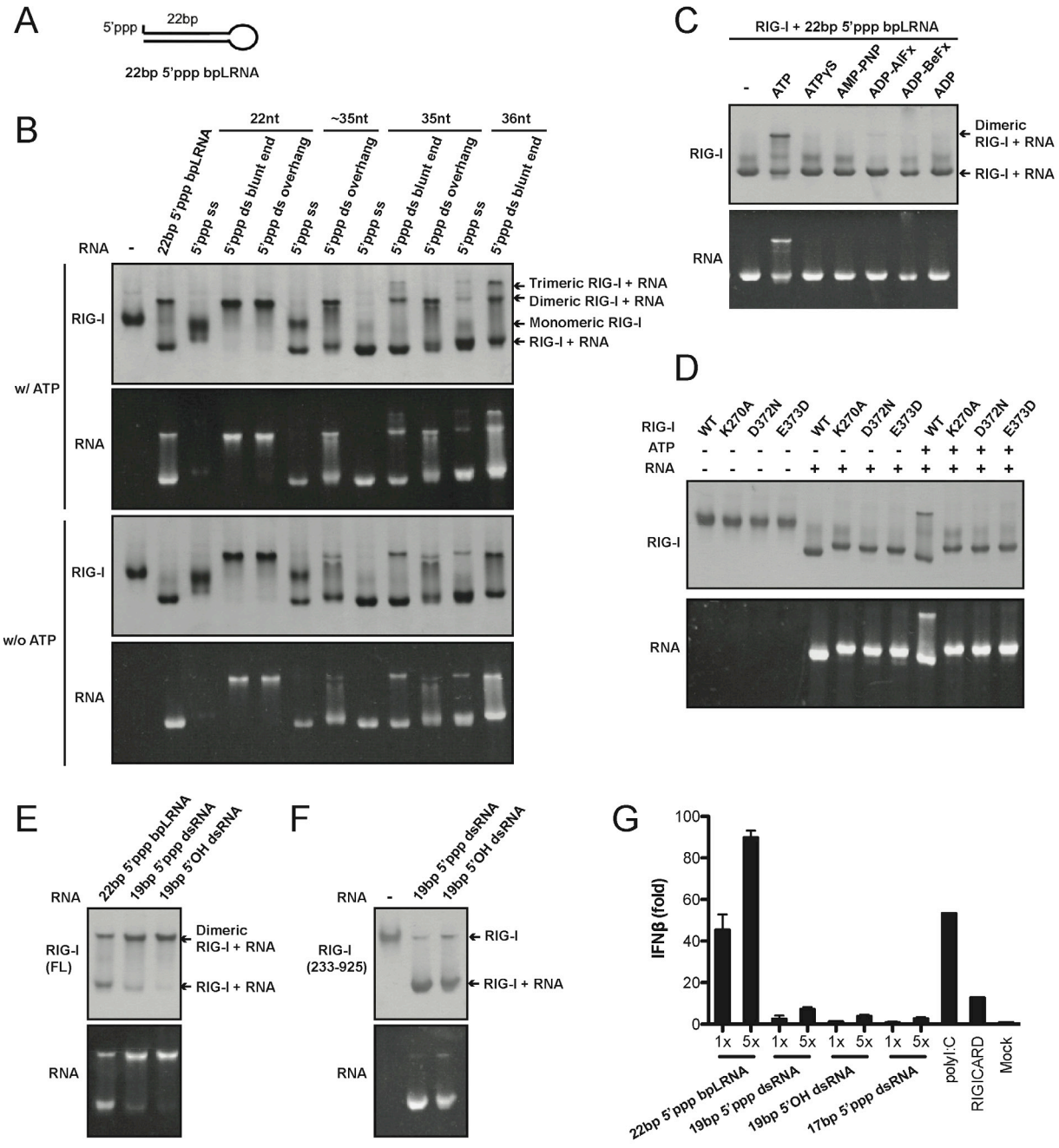

Figure 4 RIG-I oligomerization on 5'ppp dsRNA in an ATP hydrolysis-dependent and dsRNA length-dependent manner.

(A) Predicted stem-loop structure of 22bp 5'ppp bpLRNA.

(B) Binding of RIG-I with different RNAs. The complex formed by RIG-I and RNA was detected by native gel electrophoresis followed by Coomassie Blue staining of RIG-I or EB staining of RNA.

(C) RIG-I WT was not able to form dimer on 22bp 5'ppp bpLRNA in the presence of ATP non-hydrolyzable analogs or ADP.
(D) RIG-I ATPase mutants were not able to form dimer on 22bp 5'ppp bpLRNA in the presence of ATP.
(E) Binding of full-length RIG-I with different RNAs in the presence of ATP.
(F) Binding of RIG-IΔCARD with different RNAs in the presence of ATP.
(G) Different RNAs were transfected into HEK293T cells and the induced IFNβ was measured by luciferase assay.

RIG-I dimer or trimer were detected for 22bp 5'ppp bpLRNA or 35 and 36bp dsRNAs, respectively (Figure 4B). Additional bands of higher molecular weight complexes were detected using longer RNAs, such as a 135mer 5'ppp bpLRNA (data not shown). The number of RIG-I in the complex correlated well with the length of RNA suggesting a 'beads on the string' form of complex. The formation of RIG-I dimer on 22bp 5'ppp bpLRNA was dependent on ATP hydrolysis as it can not be triggered by using non-hydrolyzable ATP analogs or ADP (Figure 4C) or RIG-I ATPase mutants (Figure 4D). These results suggest that the ATP hydrolysis driven RIG-I translocation on RNA plays an important role in the formation of RIG-I oligomer.

According to the crystal structures of RNA bound form of RIG-IΔCARD (Jiang et al., 2011; Luo et al., 2011, 2012), a 19bp dsRNA is barely long enough to accommodate two RIG-IΔCARD molecules. The dimeric RIG-I/RNA complex was observed when the 19bp dsRNA was incubated with full-length RIG-I but not RIG-IΔCARD (Figures 4E and F), suggesting an important role of the N-terminal CARDs for dimer formation. Transfection of different forms of RNA into HEK293T cells expressing an IFNβ luciferase reporter plasmid showed that 19bp dsRNA has significantly weaker activity compared with 22bp 5'ppp bpLRNA (Figure 4G), although dimeric RIG-I was observed when binding to both RNAs.

This suggests that the oligomerization induced by the ATP-driven translocation of RIG-I on dsRNA may be important for IFN-β activation.

Negative stain EM structure of RIG-I/RNA complex

To study the domain arrangement of full-length RIG-I upon RNA binding, I obtained the negative stain EM map of RIG-I in complex with 22bp 5'ppp bpLRNA and ATP at ~20 Å resolution estimated by Fourier shell correlation (FSC) with the 0.5 criterion (Figure 5C). The negative stain EM map showed a rotational 2-fold symmetry with a ring shaped density at the top and a globular density at the bottom. Shortly after I obtained the negative stain EM map, several crystal structures of different domains of RIG-I were published (Table 1). The crystal structure of RIG-I helicase and CTD in complex with a dsRNA and the ATP non-hydrolyzable analog ADP-BeF_3 (PDB: 3TMI, Figure 5D) can be docked into the top ring shaped density by rigid-body fitting (Figure 5E). Superposition of the Hel-1 domains of RNA-bound and RNA-free forms of RIG-I in the EM map revealed the large conformational change at Hel-2i (yellow vs. grey, Figure 5G). In the ligand-free state, RIG-I helicase is in an open conformation (grey in Figure 5F). Hel2i and CARD2 form a substantial interface that has significant overlap with the dsRNA-Hel2i interface. The CTD, which is absent from the crystal structure of RIG-I in the RNA-free form, is flexibly linked to the helicase and remains available for sensing and capturing 5'ppp RNA with high affinity. Binding of CTD to the blunt end of bpRNA increases the local concentration of RNA in the vicinity of the helicase, favoring the interactions between helicase and dsRNA phosphate sugar backbone, thus induces the closed form of the helicase (yellow in Figure 5G). The swing of Hel2i also

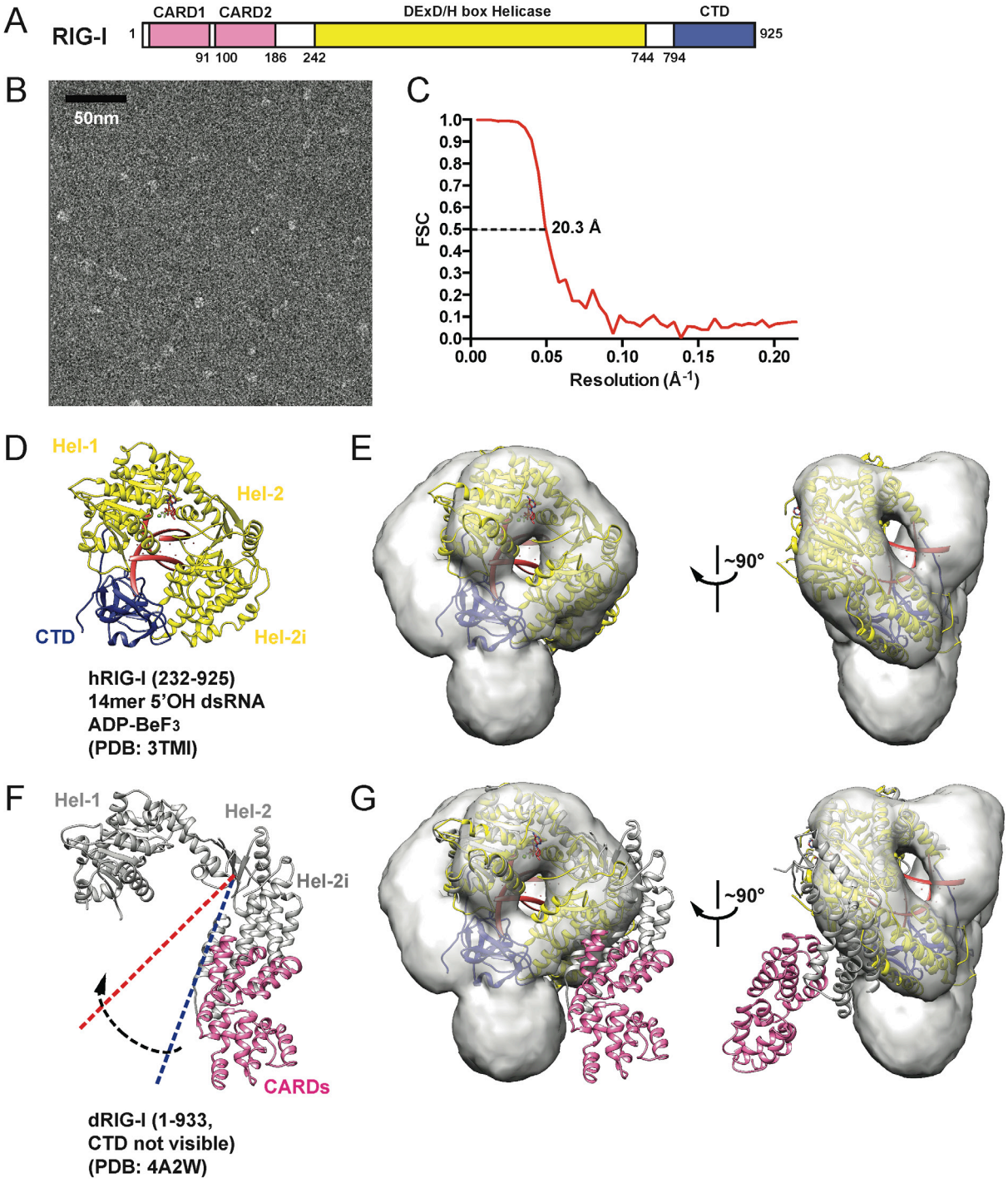

Figure 5 Negative stain EM study of RIG-I/RNA complex.
(A) Schematic representation of the domain structure of RIG-I.
(B) Negative stain EM image of the purified RIG-I in complex with 22bp 5'ppp bpLRNA and ATP. Scale bar, 50 nm.

(C) Fourier Shell Correlation (FSC) curve between maps calculated from two halves of the dataset. The dashed line points to the estimated resolution at FSC = 0.5.
(D) Crystal structure of human RIG-IΔCARDs in complex with a 14mer dsRNA and ADP-BeF_3 (PDB: 3TMI) used for rigid-body docking.
(E) Negative stain EM map of full-length RIG-I in complex with 22bp 5'ppp bpLRNA and ATP. The helicase and CTD of RIG-I in RNA bound form was docked into the ring shaped density.
(F) Crystal structure of full-length duck RIG-I in RNA free form (PDB: 4A2W). CTD is not visible in the electron density. In D and F, the Hel-1 domains (yellow and grey, respectively) are superposed to show the RNA binding induced closed conformation of Hel-2 and Hel-2i.
(G) Superposition of the Hel-1 domains of RNA bound and RNA free forms of RIG-I in the EM map.

induces the N-terminal CARDs rearranged into the globular density at the bottom of the EM map. This probably brings multiple CARDs in close proximity to facilitate subsequent ubiquitin binding.

After obtaining this negative stain EM map in late 2010, I started collecting cryoEM images of the RIG-I/22bp 5'ppp bpLRNA complex. This turned out to be challenging as the low contrast of this small complex (~220kDa) on cryoEM images and beam-induced motion limited us to obtain a large dataset. Recently, a cryoEM structure of human γ-secretase, a 170kDa membrane protein complex, at 4.5 Å resolution was reported (Lu et al., 2014). The recent revolutionary development in cryoEM with the advances of direct electron detectors and drift correction methods (Bai et al., 2013; Li et al., 2013; Scheres, 2014) may facilitate a breakthrough in this challenging project.

Oligomerization of RIG-I CARDs by K63polyUb

To elucidate the structural basis of the interaction between RIG-I CARDs and K63-linked ubiquitin chains, I synthesized and purified ubiquitin chains of different lengths and

imaged the RIG-I CARDs/Ub complex by both negative stain and cryo-EM. The protein complex dissociated heavily at the low protein concentration used to make EM grids. We then collaborated with Dr. Sun Hur's group at Harvard University to obtain the crystal structure of the RIG-I CARDs in complex with Ub_2 (Peisley et al. 2014). Binding to K63-linked ubiquitin chains induces RIG-I CARDs to form a helical tetramer resembling a 'lock-washer' (Figure 6A). The four adjacent CARDs subunits (A-D) are related by a rotation of 101° and a rise of 5Å along the central screw axis. The CARDs display exactly the same conformation as the CARDs in the monomeric RNA-free form of RIG-I. Superposition of the full-length RIG-I onto one of the CARDs subunits (A) in the tetramer shows that parts of the

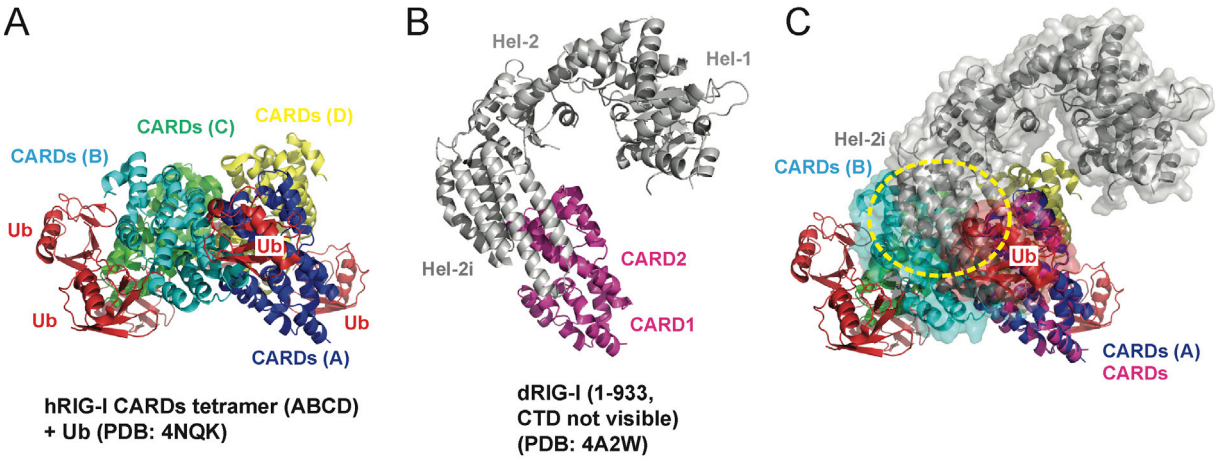

Figure 6 Domain rearrangement of RIG-I upon RNA binding is essential for ubiquitin induced RIG-I oligomerization.
(A) Crystal structure of RIG-I CARDs tetramer (chains A-D) bound by Ub chains (PDB: 4NQK) (Peisley et al., 2014).
(B) Crystal structure of full-length duck RIG-I in RNA free form (PDB: 4A2W).
(C) Superposition of full-length RIG-I onto the CARDs tetramer by aligning CARDs in full-length RIG-I (pink) with CARDs(A) (blue) in the tetramer. The same color code is used as in (A) and (B). The superposition shows that the helicase domain in full-length RIG-I masks the CARDs(A)-CARDs(B) interface as well as CARDs(A)-Ub interface, thus sterically blocks subunit A (blue) from interacting with B (cyan) and Ub. The three clashing subunits are also shown in surface representation.

CARDs-CARDs interface as well as the CARDs-Ub interface are directly masked by the helicase domain (Hel-2i) in the full-length RIG-I (Figure 6C). This reveals the importance of RNA binding induced domain rearrangement of RIG-I in the subsequent ubiquitin binding and tetramerization of RIG-I, which further activates MAVS to induce type-I interferon production.

EM reconstruction of the MAVS CARD filament

Our previous electron microscopic (EM) images of negatively stained specimens suggested that MAVS CARD assembles into a filament-like structure *in vitro* (Hou et al., 2011). To further uncover the molecular mechanism governing the MAVS CARD self-association, we utilized cryoEM to determine the molecular structure of the CARD filament. Flag-tagged MAVS CARD (residues 1-100) was expressed in HEK293T cells and purified to apparent homogeneity (Figure 7B). The purified protein formed filaments that eluted from gel filtration column in the void volume.

There are altogether 6 datasets of MAVS CARD filaments collected using different microscopes, detectors and at different magnifications (Table 2). Images were evaluated by Fourier transforms and individual datasets from different sessions of data collection were first analyzed separately. Averaged power spectra of overlapping filament segments and power spectra of 2D class averages from cryoEM images of each dataset showed the typical layer lines (Figures 8A and 9B). Considering the out-of-plane tilt of the filament sample, there is an ambiguity in the helical symmetry of the filaments (Egelman et al., 2014). So both C1 and C3 symmetries were considered and compared in the analysis.

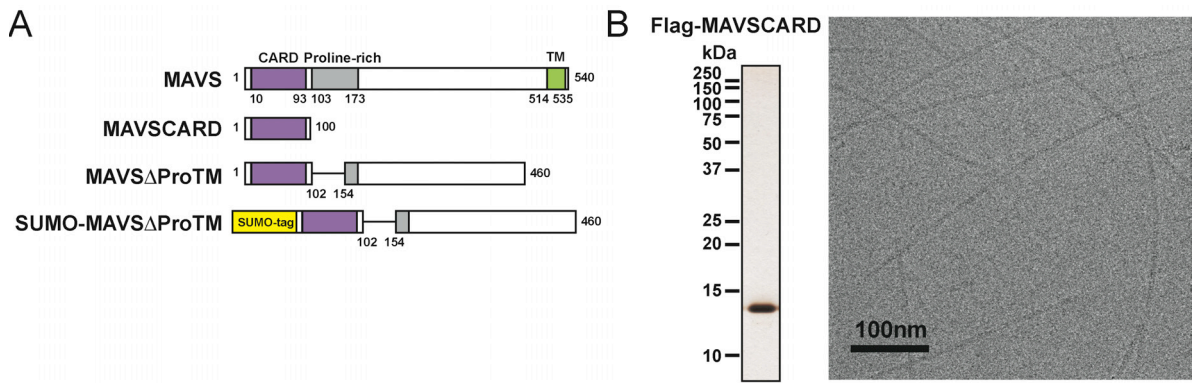

Figure 7 CryoEM sample of MAVS CARD filaments.
(A) Diagrams of the domain organization in MAVS and deletion mutants used in this study. (B) Flag-MAVS CARD purified from HEK293T cells analyzed by silver stained SDS-PAGE and cryoEM imaging.

Table 2 List of all datasets of MAVS CARD filaments

Dataset	Microscope	Detector	Mag (kx)	Pixel size calibrated (Å/pix)	No of images used	Box size (pix, Å)	No of segments
1	JEOL 2200FS FEG	Film	60	1.167	49	256, 298	24395
2	JEOL 2200FS FEG	Film	50	1.4	59	N/A	N/A
3	JEOL 2200FS FEG	Film	60	1.167	9	N/A	N/A
4	FEI Titan Krios	Falcon I	29	2.3	581	128, 294	43436
5	FEI Titan Krios	Falcon I	37	1.687	819	160, 268	96687
6	FEI Titan Krios	Falcon II	59	1.05	433 *	256, 268	27915

Note:
1. The first dataset was collected by Dr. Hui Zheng with protein purified by Dr. Fajian Hou.
2. Box size and No. of segments were used for data processing in Relion. Datasets 2 and 3 were not processed in Relion.
3. *: This is about 1/3 of data from dataset 6 that was processed at the time of writing this thesis.

Images from datasets 1-4 were first processed by Dr. Qiu-Xing Jiang using the Iterative Helical Real Space Reconstruction (IHRSR) method (Egelman, 2010) implemented in SPIDER. Datasets 1-4 were merged together by interpolating and scaling images

according to the layer lines and symmetry parameters (Δz). After rescaling datasets 2-4 according to dataset 1, the position of layer line 9 in the averaged power spectrum is at ~1/(17Å) according to the 1.167 Å calibrated pixel size of dataset 1 (Figure 8A). The initial helical parameters (the axial rise, Δz, and the azimuthal rotation, ΔΦ) used for C1 and C3 symmetries were (4.75Å, -101.25°) and (16.5Å, -53.33°), respectively. The IHRSR analysis of the merged dataset started with a featureless cylinder as the initial reference (Figure 8B) and converged to a stable solution at C3 symmetry (Xu et al., 2014). After sorting the filaments to consider variations in helical symmetry and out-of-plane tilt by up to 15°, about ~31.4% data (15,366/48,884 boxed segments of filaments) was used to generate a cryoEM map with C3 symmetry at ~9.6 Å resolution (Figure 8C; Xu et al., 2014). The cryoEM map shows a three-stranded helical assembly with a central pore that is about 18 Å in diameter. Neighboring subunits in each strand are related by an azimuthal rotation (ΔΦ) of -53.6° and an axial rise (Δz) of 16.8 Å along the helical axis (Figure 8C).

To obtain a higher resolution map, we recently collected a high resolution dataset (dataset 6) using automated data acquisition in an FEI Titan Krios with a Falcon II direct electron detector in November, 2014. I learned the data processing of helical filaments using a recently developed method (Clemens et al, 2015). Images were processed using a customized version of Relion (Scheres et al., 2012; Clemens et al, 2015) developed by Dr. Peng Ge in Dr. Z. Hong Zhou lab at UCLA. This 'helical' Relion has an implementation of the IHRSR method based on the framework of Relion 1.2. Prior to 3D classification, individual datasets were subjected to reference-free 2D classification (Table 3). Class averages of some of the highly populated classes showed some nice features of the helical

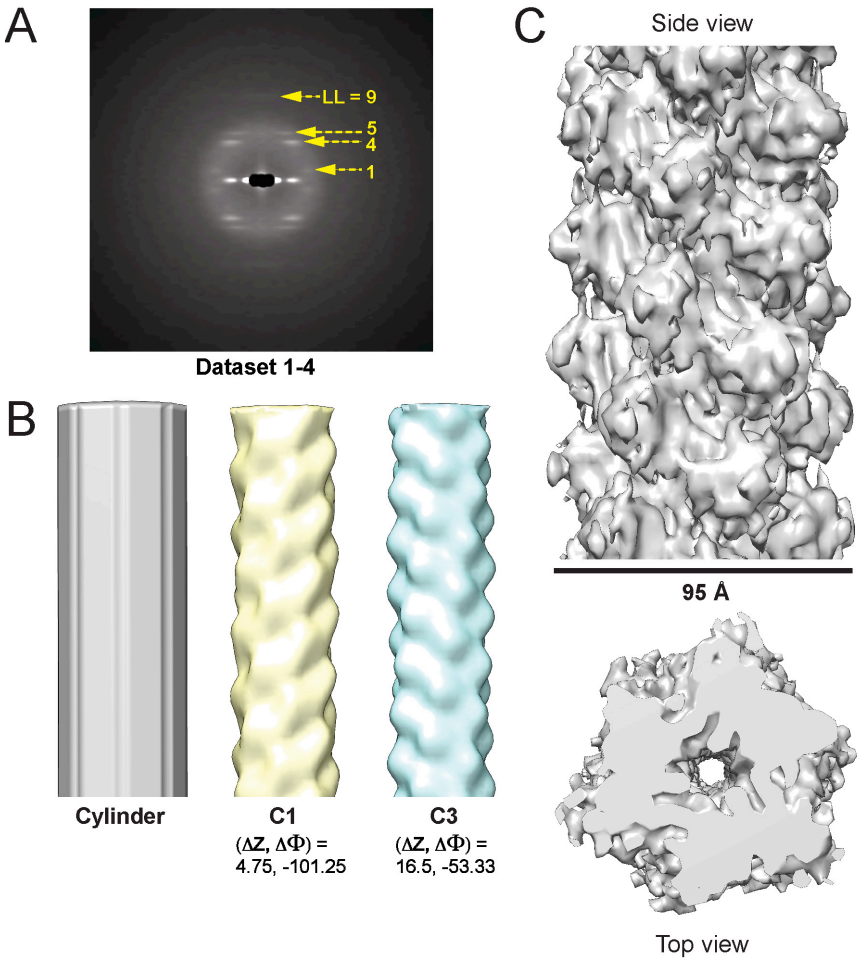

Figure 8 CryoEM reconstruction of MAVS CARD filaments using datasets 1-4. (Xu et al., 2014)
(A) Averaged power spectrum calculated from datasets 1-4.
(B) Reference maps used for 3D reconstruction.
(C) Views of the C3 map of MAVS CARD filament. The C3 map was generated using a subset of sorted filaments from datasets 1-4 and calculated in SPIDER.

filaments (Figure 9A) and good classes showing clear layer lines were selected (Figure 9B). For dataset 6, 15,600 out of 27,915 boxed segments of filaments were used to calculate the refined map. The refinement converged at a C1 helical symmetry with an azimuthal rotation (ΔΦ) of -101.21° and an axial rise (Δz) of 5.06 Å (Figures 9C and 13; movie 1). The final map has an overall resolution of 4.25 Å, estimated by Fourier Shell Correlation (FSC) using

the FSC=0.5 criterion (Figure 9F). To evaluate the map using an independent method, a B-factor weighted PDB-based map was calculated to 4.1 Å and used to calculate FSC with the experimental map. A 0.5 threshold found an estimated resolution of 4.25 Å (Figure 9G), close to the one estimated using two halves of experimental data (Figure 9F). Datasets 4 and 5 were also processed in the same manner. Dataset 5 collected in May 2013 is the largest dataset. The C1 map calculated from dataset 5 (Figure 9C) has an overall resolution of 6.5 Å,

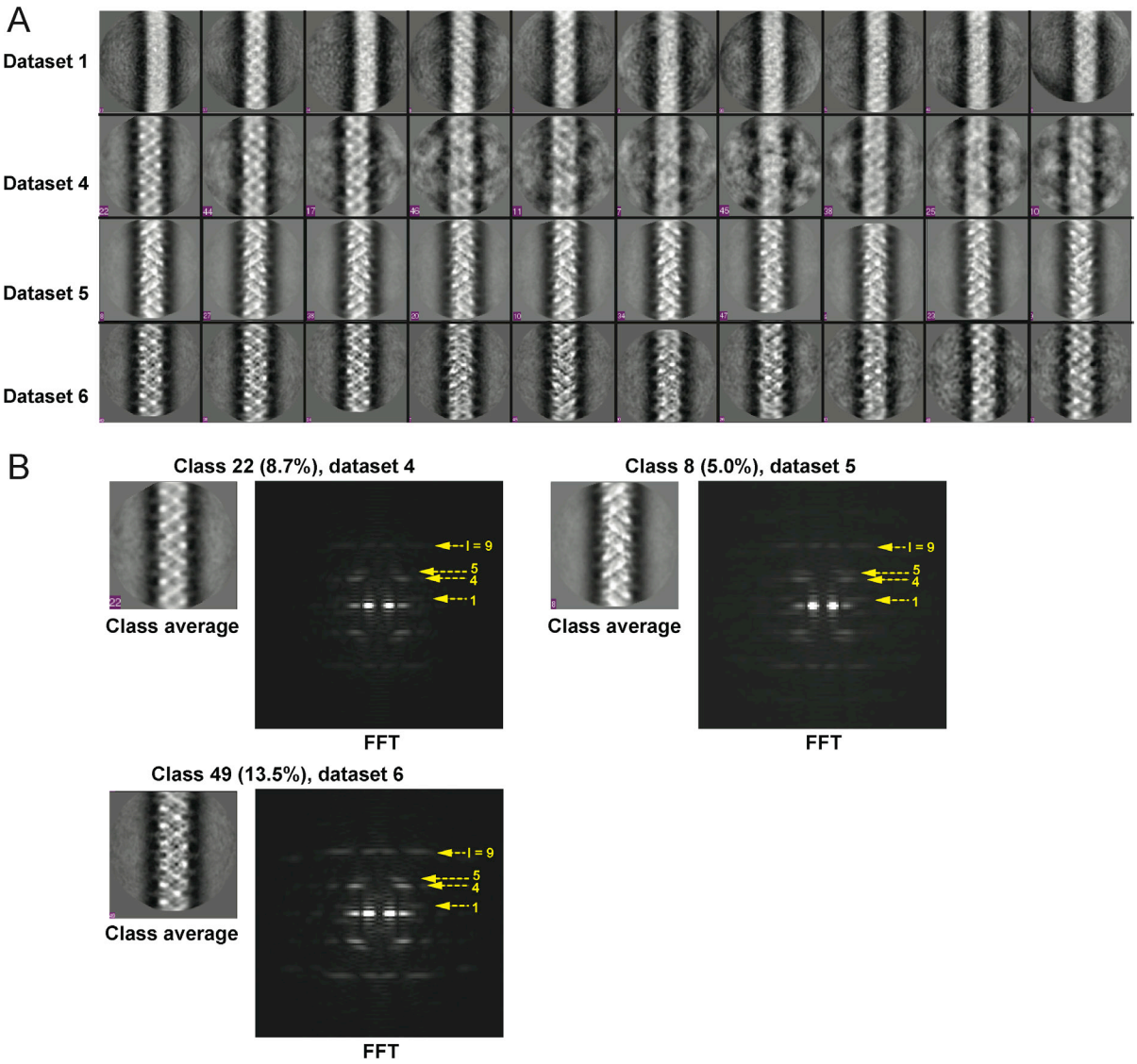

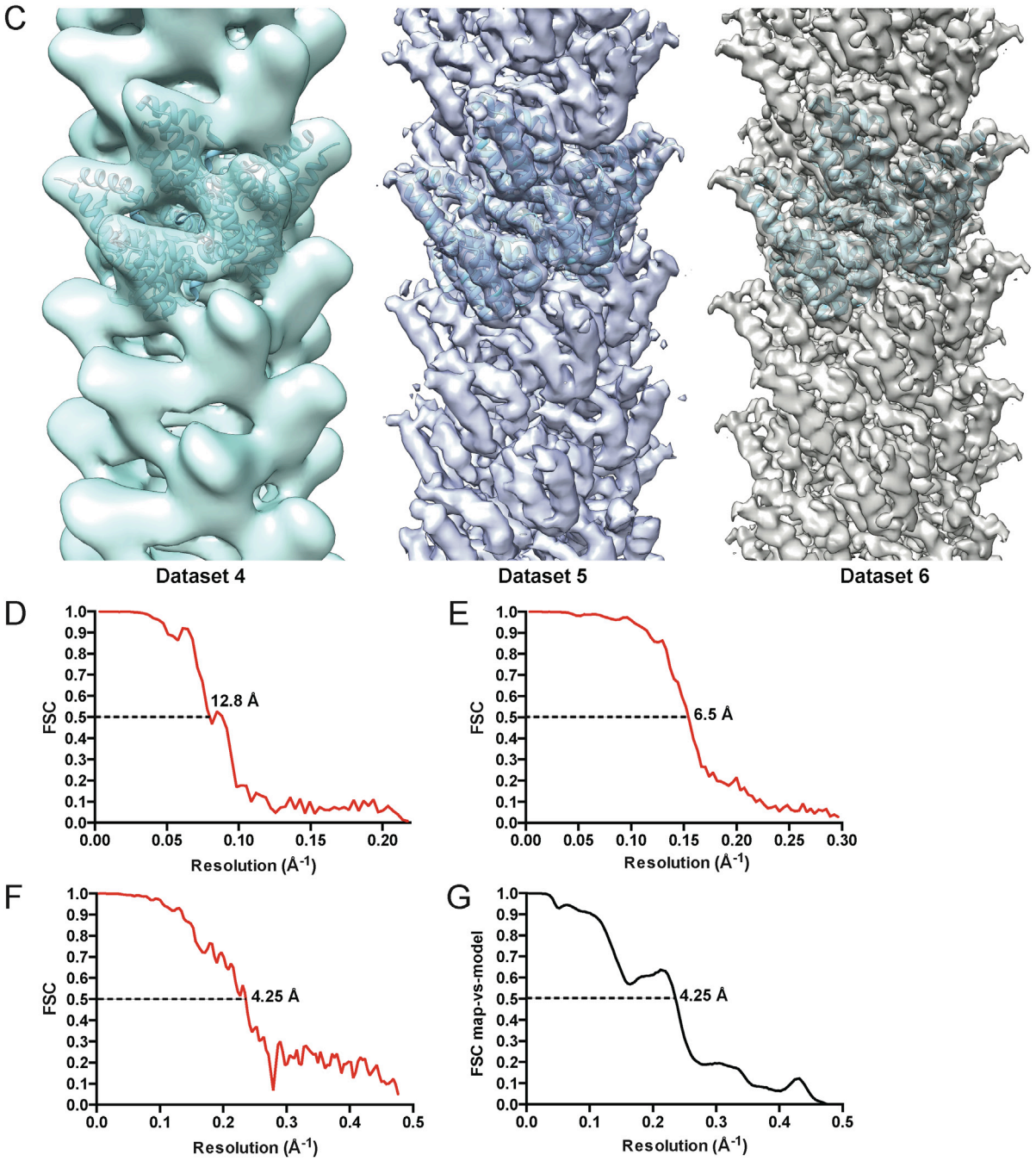

Figure 9 CryoEM reconstruction of MAVS CARD filaments from different datasets processed using a customized Relion.

(A) 2D class averages of the top 10 most populated classes of different datasets.

(B) 2D class averages of the most populated class of different datasets and the power spectra.

(C) Side view of the C1 maps of MAVS CARD filament calculated from datasets 4, 5 and 6 using a customized Relion developed by Dr. Peng Ge at UCLA, with the atomic model (residues 1-97) docked in.
(D-F) Fourier Shell Correlation (FSC) curves between maps calculated from two halves of the dataset for datasets 4, 5 and 6, respectively. The dashed line points to the estimated resolution at FSC = 0.5.
(G) FSC between the segmented cryoEM map of one CARD from dataset 6 and the map calculated from the atomic model (residues 1-97). The resolution was estimated with FSC = 0.5 threshold.

estimated by Fourier Shell Correlation (FSC) using the FSC=0.5 criterion (Figure 9E). The C1 map from dataset 4 displayed an azimuthal rotation (ΔΦ) of -101.26° and an axial rise (Δz) of 5.28 Å and has an estimated resolution of 12.8 Å (Figures 9C and D). Notably, there are some differences in Δz of C1 maps calculated from individual datasets. For example, the position of layer line 9 in the averaged power spectra of datasets 5 and 6 is at ~1/(18Å) according to the 1.05 Å calibrated pixel size of dataset 6, while it is at ~1/(17Å) according to the 1.167 Å calibrated pixel size of dataset 1. This suggested that the pixel sizes calibrated in different imaging systems might be off slightly (~5%).

Recently, another group also reported a high-resolution cryoEM reconstruction of MAVS CARD filaments (Wu et al., 2014). Despite many differences in experimental conditions (e.g. protein construct, expression and purification), the reported cryoEM map displayed a similar C1 helical symmetry with the high-resolution C1 maps we obtained. Currently only about 1/3 of images in dataset 6 were processed to generate the 4.25 Å map. Although it is possible that a higher resolution model may be obtained when the entire dataset is analyzed, the structural details observed in the cryoEM map, including clearly observed secondary structures and many side-chain densities (Figures 9C and 13; movie 1), have provided a sufficient validation of the C1 structure.

Table 3 2D Classification in Relion

	Set01				Set04			
	No of segments: 24395 Pixel size: 1.167 Å/pix Resolution of 2D classification: 6.64 Å				No of segments: 43436 Pixel size: 2.3 Å/pix Resolution of 2D classification: 4.67 Å			
Sort	Class	Distribution (%)	Accuracy Rotation	Accuracy Translation	Class	Distribution (%)	Accuracy Rotation	Accuracy Translation
1	33	6.29	2.55	2.23	22	8.67	1.48	0.61
2	37	5.97	2.30	2.35	44	5.76	1.28	0.56
3	24	5.11	2.70	2.85	17	5.26	1.28	0.59
4	8	4.95	2.55	2.65	46	3.96	1.09	0.59
5	0	4.75	2.30	2.50	11	3.89	1.11	0.62
6	18	4.28	2.60	2.95	7	3.48	1.09	0.56
7	36	4.18	2.45	2.45	45	3.40	1.09	0.63
8	25	4.14	2.11	2.19	38	2.92	1.08	0.62
9	46	4.11	2.13	2.21	25	2.84	0.90	0.52
10	48	3.85	2.15	2.16	10	2.73	0.90	0.56

	Set05				Set06			
	No of segments: 96687 Pixel size: 1.687 Å/pix Resolution of 2D classification: 3.42 Å				No of segments: 27915 Pixel size: 1.05 Å/pix Resolution of 2D classification: 5.07 Å			
Sort	Class	Distribution (%)	Accuracy Rotation	Accuracy Translation	Class	Distribution (%)	Accuracy Rotation	Accuracy Translation
1	8	5.03	1.34	0.73	49	13.49	2.15	2.13
2	27	4.96	1.30	0.74	38	10.47	2.60	2.19
3	38	4.45	0.90	0.69	24	9.01	2.60	2.30
4	20	4.07	1.30	0.73	7	7.74	2.10	2.01
5	10	3.94	1.30	0.74	45	7.01	1.90	1.96
6	34	3.90	1.30	0.73	20	6.23	2.30	2.28
7	47	3.83	1.38	0.74	26	5.43	2.60	2.55
8	4	3.80	1.30	0.73	40	3.63	2.60	2.70
9	23	3.56	1.07	0.69	48	3.52	3.10	3.45
10	9	3.55	1.30	0.73	43	3.42	2.60	2.75

Due to the limited resolution of the C3 map obtained in the early studies and the high-resolution C1 maps, it was argued that C3 is not the right symmetry for MAVS CARD filaments (Egelman et al., 2014; Wu et al., 2014). The C1 maps we obtained from datasets 4, 5 and 6 also make it a necessity to reanalyze the earlier datasets by considering and comparing both possibilities of C1 and C3 filaments. We recently performed 3D classifications with two classes using the C1 and C3 maps as two reference models. This

parallel sorting may identify structurally homogeneous subsets. Consistent with the 3D reconstruction, for datasets 5 and 6, the majority of filament segments were classified as C1 filaments. Interestingly, for both datasets 1 and 4, subsets of images showed higher cross-correlation with references generated from the C3 map. Filaments agreed with the C1 model might be excluded in the previous analysis to calculate the C3 map when datasets were sorted into nine bins by aligning them against C3 models with symmetry parameters centered around ($\Delta\Phi$ = -53.6°, Δz = 16.5 Å) with $\Delta\Delta\Phi$ = 2.0° and $\Delta\Delta z$ = 1.5 Å by considering variations in C3 helical symmetry and out-of-plane tilts (Xu et al., 2014). Using the C3 map as reference for 3D classification and refinement with C3 symmetry parameters, the sorted filaments from dataset 4 can converge at a C3 helical symmetry of an azimuthal rotation ($\Delta\Phi$) of -53.2° and an axial rise (Δz) of 18.6 Å (the 18.6 Å rise was based on the 2.3 Å calibrated pixel size of dataset 4; while for the previous analysis in SPIDER, the 16.5 Å rise was based on the rescaled pixel size against dataset 1). However, the resolution of the C3 map calculated from the sorted data was still limited. I am going to compare the C3 and C1 maps in different aspects.

Rigid-body assembly of MAVS CARDs in the filaments

Although the MAVS filaments share some features with prion fibers, such as self-perpetuation, they could not be stained with Congo red, a dye commonly used to label β-sheet-rich insoluble amyloid aggregates formed by most prions (Hou et al., 2011). MAVS CARD lacks the glutamine/asparagine-rich regions that are responsible for forming the cross-beta structures of most amyloid fibers (Michelitsch and Weissman, 2000; Nelson et al.,

2005). There is no evidence that during filament formation MAVS CARD undergoes a helix-to-beta-sheet transition in its secondary structure. I therefore first performed rigid-body docking of the crystal structure of individual MAVS CARD (residues 3-93) (Potter et al., 2008) and the atomic model of residues 1-97 (Wu et al., 2014) into the reconstructed cryoEM maps.

Before obtaining the high-resolution datasets, we collaborated with Dr. Zhiheng Yu at HHMI Janelia Farm Research Campus and obtained cryo-electron tomograms (cryo-ET) of the CARD filaments to determine the handedness of the helical assembly of MAVS CARD. Figure 10 shows a 2.7 nm-thick slice of the tomogram as viewed from the outer surface of

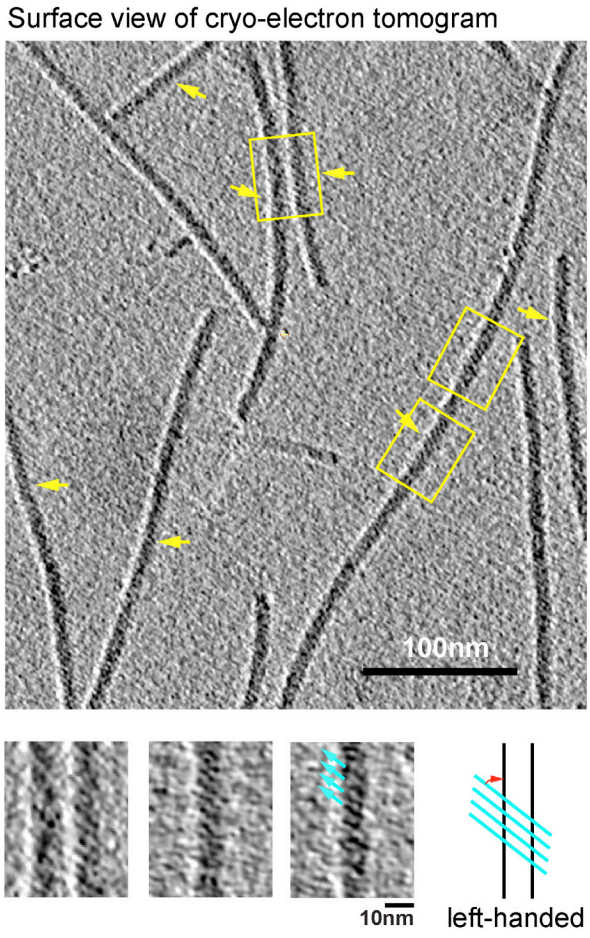

Figure 10 Chirality determination by cryo-electron tomography (cryo-ET).

The projection image calculated from a 2.7 nm slice out of the cryo-ET reconstruction as viewed from the outer surface of the filaments. Yellow arrows point to portions of multiple filaments where apparent helical stripes were resolved. Three zoomed-in views from filaments of different orientations display a well-matched left-handedness with the cryo-EM map.

the filaments. Apparent helical stripes observed in multiple filaments of different orientations suggest that the helical filament is left-handed. The measured vertical distance between adjacent stripes from the cryo-ET reconstruction is approximately 38 Å, matching well with both the C3 and C1 maps at the current resolution. The measured angle between the strips and the helical axis is ~50°. The left-handedness of the filaments was also confirmed by Freeze-etch EM study performed by Ms Robyn Roth at Washington University at St Louis.

Interactions in MAVS CARD filaments based on the C3 map

Docking of the crystal structure into the C3 map was mainly based on the three rod-shaped EM densities at the peripheral surface of the cryoEM map (Figure 8C). Three α-helices (H1, H4 and H3) were positioned into the rod-shaped densities. In the structural model based on the C3 filament, each MAVS CARD monomer directly interacts with four nearby monomers: two from the same strand and the other two respectively from two adjacent strands (Figure 11B). Within one layer perpendicular to the helical axis, the three subunits do not make direct contact with each other. Two types of interfaces are involved in the packing interactions. The intra-strand interface makes contacts between adjacent CARDs within the same strand (Figure 11D) while the inter-strand interface holds the three strands together (Figure 11C).

Inter-strand interface

At the inter-strand interface, the positive and negative charges are distributed at two opposite ends of each CARD subunit, indicating that the inter-strand interaction is mainly

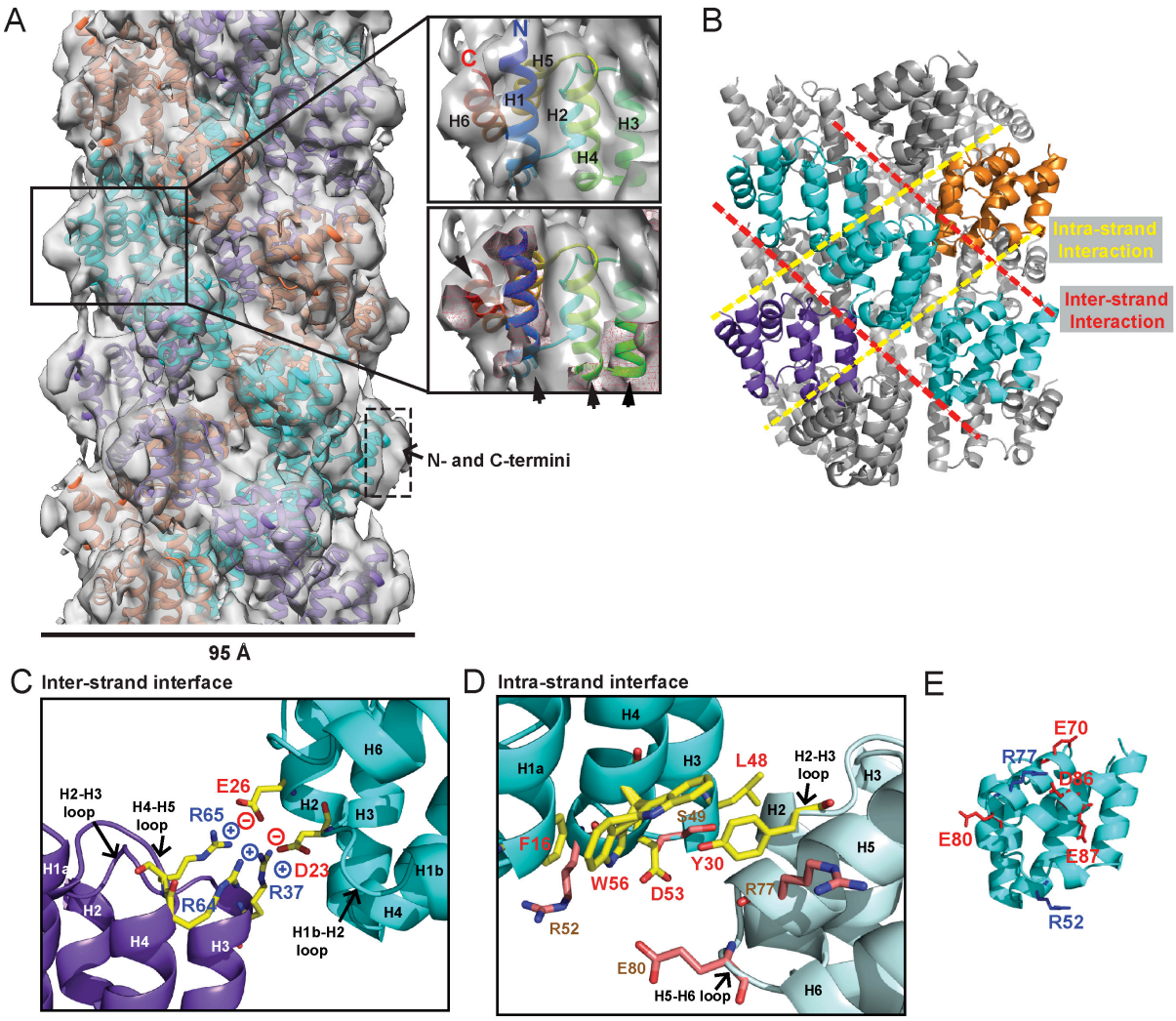

Figure 11 Residues at the inter- and intra-strand interfaces based on the C3 map.
(A) A side view of the C3 map of MAVS CARD filament with the crystal structure of human MAVS CARD (PDB: 2VGQ) docked in by rigid-body fitting. Three strands are colored differently.
(B) Pseudoatomic model of MAVS CARD filament based on the C3 map. Dashed lines indicate the inter- (red) and intra-strand (yellow) interaction interfaces.
(C) The inter-strand interface between two subunits (purple and cyan) with key residues shown as yellow sticks. The side chains of residues D23, E26, R37, R64 and R65 in the model were optimized by testing different rotamers in COOT.
(D) The intra-strand interface between two subunits (cyan and palecyan) with key residues shown as yellow sticks.
(E) Surface-exposed, conserved charged residues shown as sticks (blue, positively charged residues; red, negatively charged residues).

electrostatic (Figure 11C). The positively charged residues R37 in the 3rd helix (H3), R64 and R65 in the loop between the 4th and 5th helices (H4 and H5) from the CARD in a lower layer (purple in Figure 11C) are in close proximity to the negatively charged residues D23 in the loop between the 1st and 2nd helices (H1b and H2) and E26 in the 2nd helix (H2) of another CARD molecule (cyan in Figure 11C) in the upper layer. E26, R64 and R65 are highly conserved among MAVS molecules from different species, but D23 and R37 are less so (Figure 12). Replacement of D23 with a histidine residue and R37 with either an asparagine or a serine residue in the MAVS orthologs introduces good H-bonders to these less conserved positions, and may compensate for the lost electrostatic pairs.

Intra-strand interface

The intra-strand interface based on the C3 map may be mediated by a combination of aromatic-aromatic, hydrophobic interactions and hydrogen bonding among residues F16, W56, Y30, D53 and L48 (Figure 11D). W56 is well conserved (leucine in horse). In the crystal structure of MAVS CARD, the side chain of W56 adopts different conformations, with a major conformer (60% occupancy) exposed to solvent and stacked against the aromatic ring of residue F16 in immediate vicinity (Potter et al., 2008). Y30 is a fairly conserved residue (histidine in cattle) that protrudes to the close proximity of W56 in the other CARD molecule at the interface. D53 is one helical turn below W56, and its side chain sits at the boundary between the aqueous phase and the packing of F16, W56 and Y30. Close to the central pore of the helical filament, residue L48 appears in close contact with a group of short chain residues and contributes to a separate hydrophobic patch.

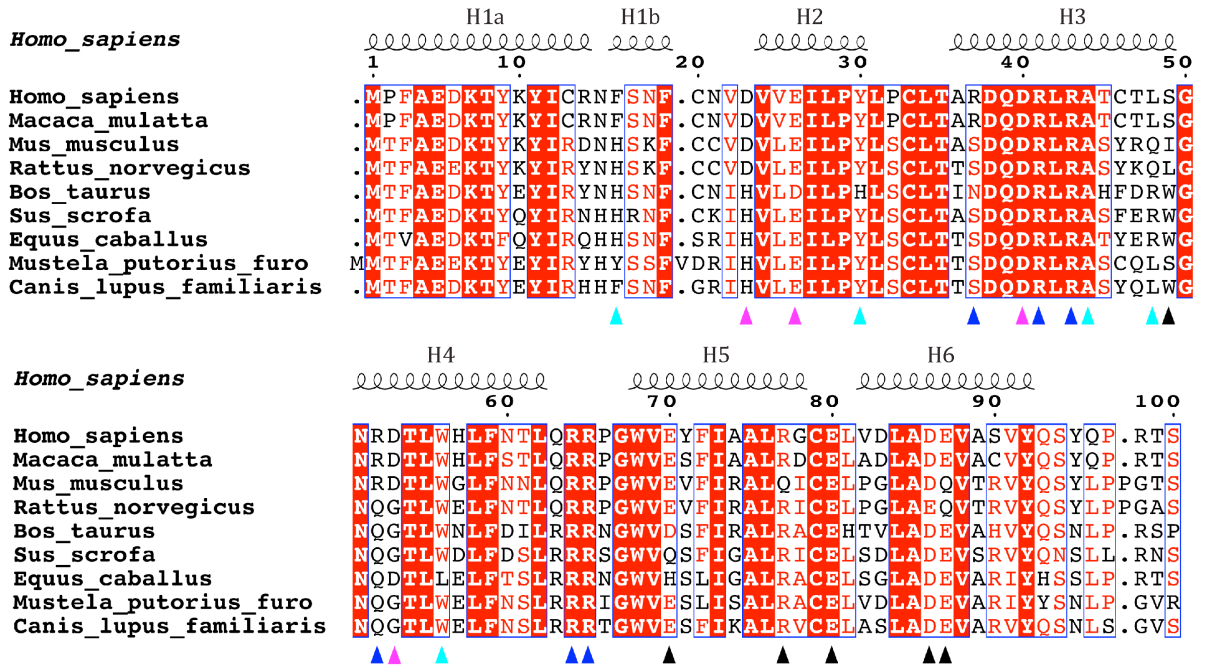

Figure 12 Sequence alignment of MAVS CARD from 10 different species with the secondary structures based on the crystal structure of human MAVS CARD.
The alignment was generated with ClustalW (http://www.ebi.ac.uk/clustalw/) and formatted using ESPript (http://espript.ibcp.fr/ESPript/ESPript/). The colored arrowheads mark the residues mutated in this study: pink, key negatively charged residues; blue, key positively charged residues; cyan, key hydrophobic and hydrophilic residues; black, residues showing normal activity when substituted with alanine.

Interactions in MAVS CARD filaments based on the C1 map

EM densities of the six α-helices of each CARD molecule are well resolved in the high-resolution C1 map (Figure 13). High resolution of the density map not only enables unambiguous identification of the orientation of individual CARDs within the filament, but also showed clear grooves in α-helices and multiple bulky side chains (Figures 13 and 14, movie 1). The atomic models of MAVS CARD (Potter et al., 2008; Wu et al., 2014) were first docked into the density by rigid-body fitting and adjusted in COOT. Except for some of the loop regions, the six α-helices fit into the EM density very well suggesting that the

filament is formed through rigid-body assembly. While the six α-helices of the crystal structure of MAVS CARD monomer (PDB: 2VGQ, residues 3-93) fitted into the EM map well, multiple bulky side chains and those residues in the loop between H4 and H5 needed adjustment (Figure 14). The final model after refinement showed a nearly identical conformation as the atomic model reported previously (PDB: 3J6J, residues 1-97, Wu et al., 2014).

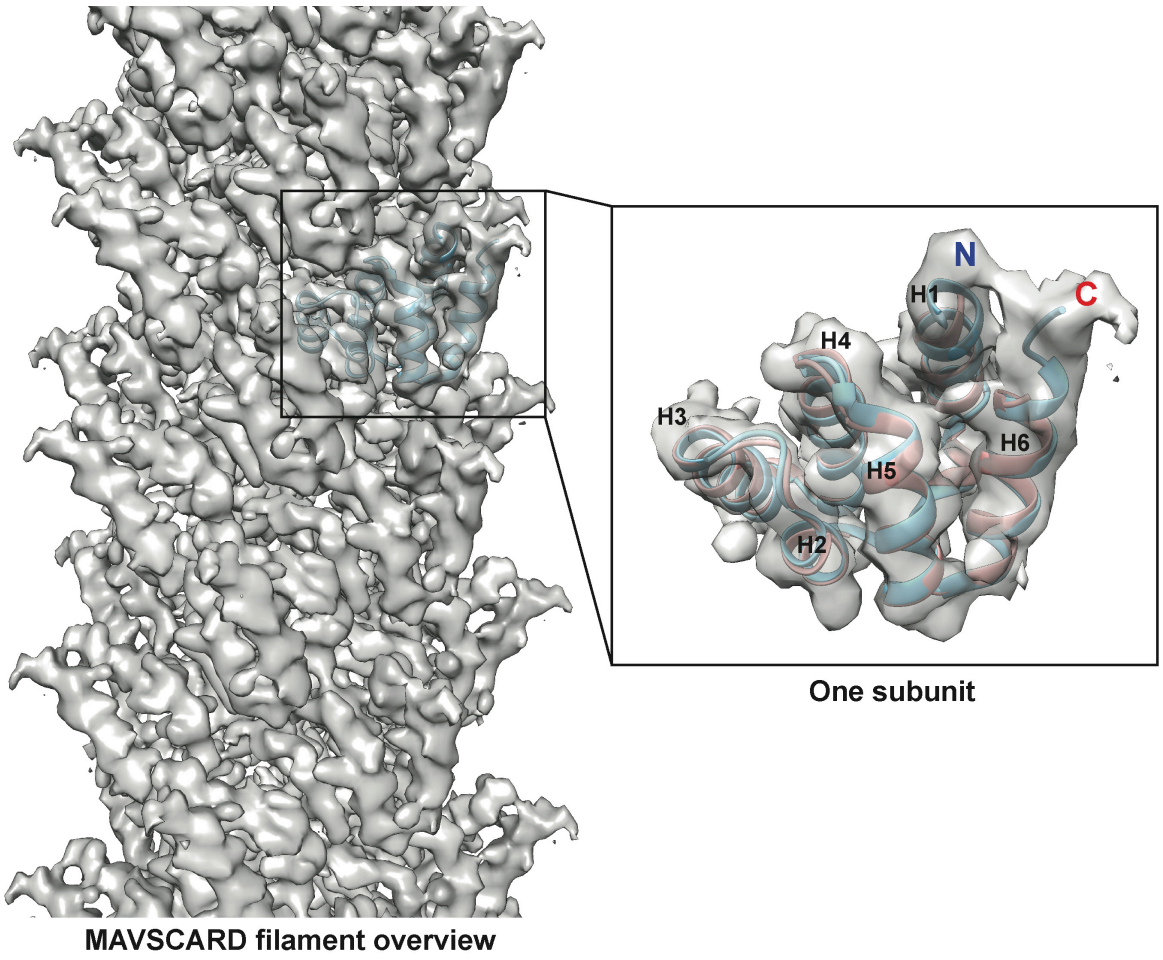

Figure 13 CryoEM reconstruction of MAVS CARD filaments at 4.25 Å resolution.
A side view of the C1 map of MAVS CARD filament obtained from dataset 6 with atomic models of human MAVS CARD docked into the cryoEM map (pink: crystal structure of residues 3-93, PDB: 2VGQ; blue: atomic model of residues 1-97, built based on PDB: 3J6J

by rigid-body fitting using the program Chimera followed by side chain refinement using the program COOT). The N- and C-termini face the periphery of the filament.

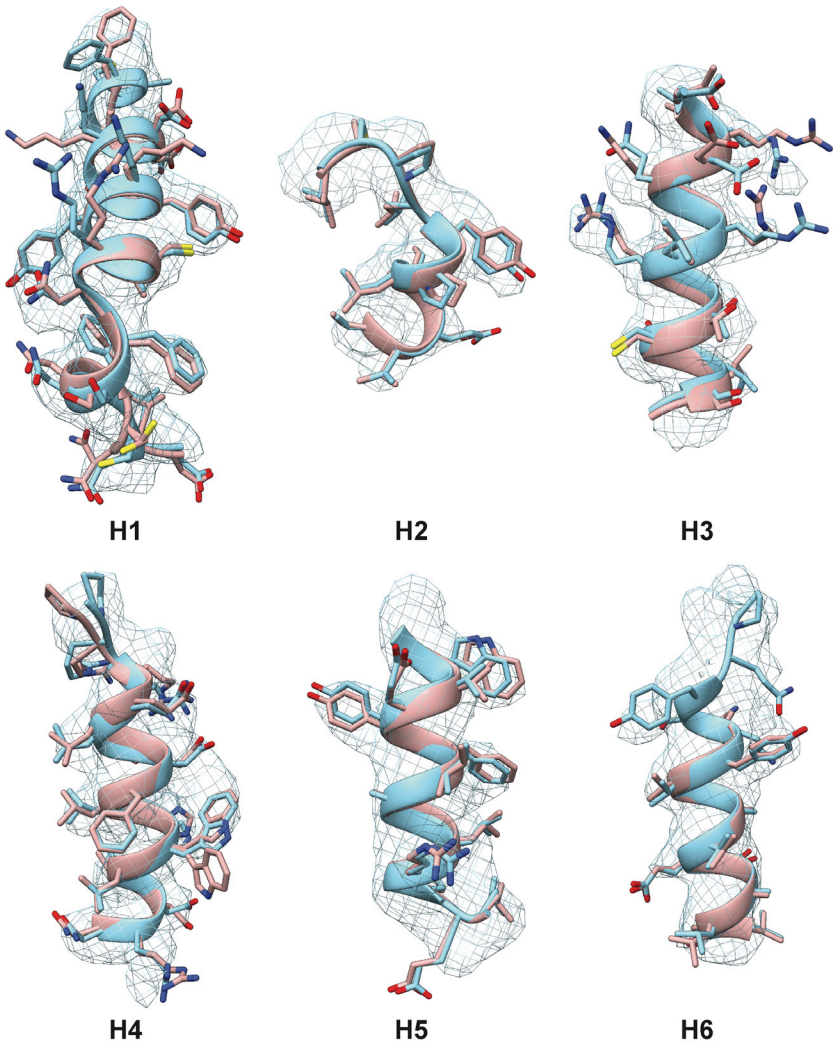

Figure 14 Zoomed-in views of the six α-helices with side chains shown as stick models and superimposed with the EM density of the C1 map generated from dataset 6 (The same color code is used as in Figure 13; pink: crystal structure of residues 3-93, PDB: 2VGQ; blue: atomic model of residues 1-97).

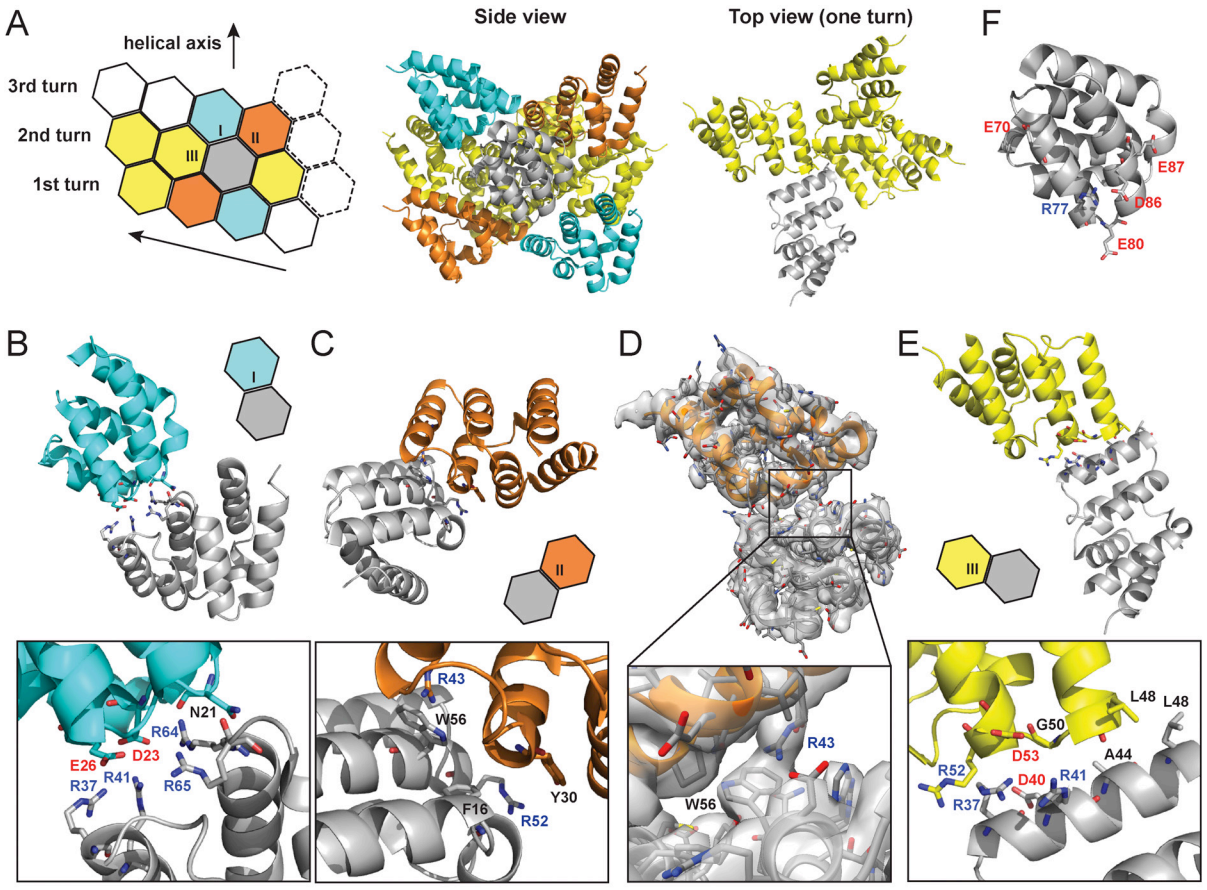

Figure 15 Residues at the interfaces based on the C1 map.
(A) A model of MAVS CARD filament based on the cryoEM map, showing three helical turns. Each MAVS CARD interacts with six nearest neighbors: two neighbors along the helical trajectory (grey and yellow), and four neighbors between helical turns (grey and cyan, grey and orange).
(B-C) Details of interactions at type I and II interfaces. Residues at the interfaces are shown as stick models.
(D) The segmented EM map with two MAVS CARD molecules and the magnified view of type II interface with clear EM density for W56 and R43.
(E) Details of interactions at type III interface. Residues at the interface are shown as stick models.
(F) Surface-exposed, conserved charged residues shown as sticks (blue, positively charged residues; red, negatively charged residues). Mutations of these surface residues did not impair MAVS signaling.

In the structural model of the filament, each MAVS CARD monomer interacts with six nearby monomers through three types of intermolecular interactions (I, II and III) (Figure 15A).

Interface I

At interface I, the positive and negative charges are distributed at two opposite ends of each CARD subunit, indicating that this interface is mainly mediated by electrostatic interactions (Figure 15B). The positively charged residues R37 and R41 in the 3rd helix (H3), R64 and R65 in the loop between the 4th and 5th helices (H4 and H5) from one CARD molecule (grey in Figure 15B) are in close proximity to the negatively charged residues D23 in the loop between the 1st and 2nd helices (H1b and H2) and E26 in the 2nd helix (H2) of another CARD molecule (cyan in Figure 15B). The charged residues at this interface are also the ones at the inter-strand interface of the C3 map.

Interface II

The cryoEM model predicts that interface II is mediated by a combination of electrostatic, hydrophobic interactions and hydrogen bonding among residues F16, W56, R43, Y30 and R52 (Figure 15C). W56 is well conserved (leucine in horse). As mentioned earlier, the side chain of W56 adopts different conformations as shown in the crystal structure of MAVS CARD (pink in the zoomed-in view in Figure 14) (Potter et al., 2008). In the cryoEM map, the density of one conformer is resolved (Figure 14) and there appears a clear density corresponding to the side chain of R43 from an adjacent CARD (Figures 15D),

suggesting a direct cation-pi interaction between these two residues. Y30 is a fairly conserved residue (histidine in cattle) at the interface.

Interface III

Interface III mediates the interactions between adjacent monomers along the helical trajectory. Close to the central pore of the helical filament, residue L48 from each MAVS CARD monomer forms a hydrophobic core with G50 and A44 in close proximity (Figures 15A, top view and 15E). Charged residues R37, R41, D40 and D53 are located at the outer rim of the filament forming electrostatic interactions together with charged residues at type I interface.

In both models from the C3 and C1 maps, the first (H1) and last (H6) helices of the CARD are positioned at the outer surface of the filament (Figures 11A and 13). This arrangement provides the structural basis for other domains to be connected to the filaments in the center, in keeping with previous observations that an N-terminal small ubiquitin-like modifier (SUMO) tag and other domains added to the C-terminus of CARD did not prevent filament formation (Hou et al., 2011). There are some unoccupied densities next to the N- and C-termini of the docked CARD model (Figures 11A, 13 and 14). These extra densities may be due to the residues from the N-terminal Flag tag and the additional residues at the C-terminus of the protein used for preparing the cryoEM specimens; these extra residues are not present in the proteins shown in the atomic models. Based on our pseudoatomic models, residues in the first helix (H1) are not in direct contact with any adjacent molecule (Figures

11A and 13). This agrees with our previous finding that deletion of the first ten residues in MAVS CARD did not impair its filament formation (Hou et al., 2011). In addition, no cysteine pairs are at the interface, which explains the prior observation that MAVS filaments were not disrupted by a high concentration of reducing agent DTT (Hou et al., 2011).

Structure-based mutagenesis in cells for MAVS signaling

Although the detailed interactions at the interfaces are different according to the C3 and C1 maps, key residues involved in the interactions are almost identical revealed by these two models.

To test the important residues at the interfaces, structure-guided mutagenesis was performed and the *in vivo* signaling activity of MAVS induced by MAVS CARD polymerization was tested. The cDNAs encoding these MAVS mutants were transiently expressed in HEK293T cells together with an IFNβ luciferase reporter plasmid. IFNβ induction was measured by a luciferase assay.

At interface I of the C1 model, the charged residues were mutated individually to an alanine residue or residues with reversed charges to test the energetic contributions of them to the stability of the filament and the *in vivo* MAVS signaling activity. Compared with the wild-type MAVS, which potently induced IFNβ in a dose-dependent manner, D23A showed significantly decreased activity and mutations of the other charged residues (E26, R37, R41, R64 and R65) at the interface almost completely abolished MAVS activity (Figures 16A and B).

At interface II, alanine substitution of W56 and R43 almost completely abolished MAVS activity. In addition to W56, the ring structures of residues F16 and Y30 also appear to be important for filament assembly. Single alanine substitution of F16, W56 or Y30 almost completely abolished MAVS activity, while substitution with different ring-containing residues to these positions, such as F16H, W56F, W56Y, Y30F and Y30H, was able to largely rescue MAVS activity (Figure 16B). Another residue involved in stabilizing the

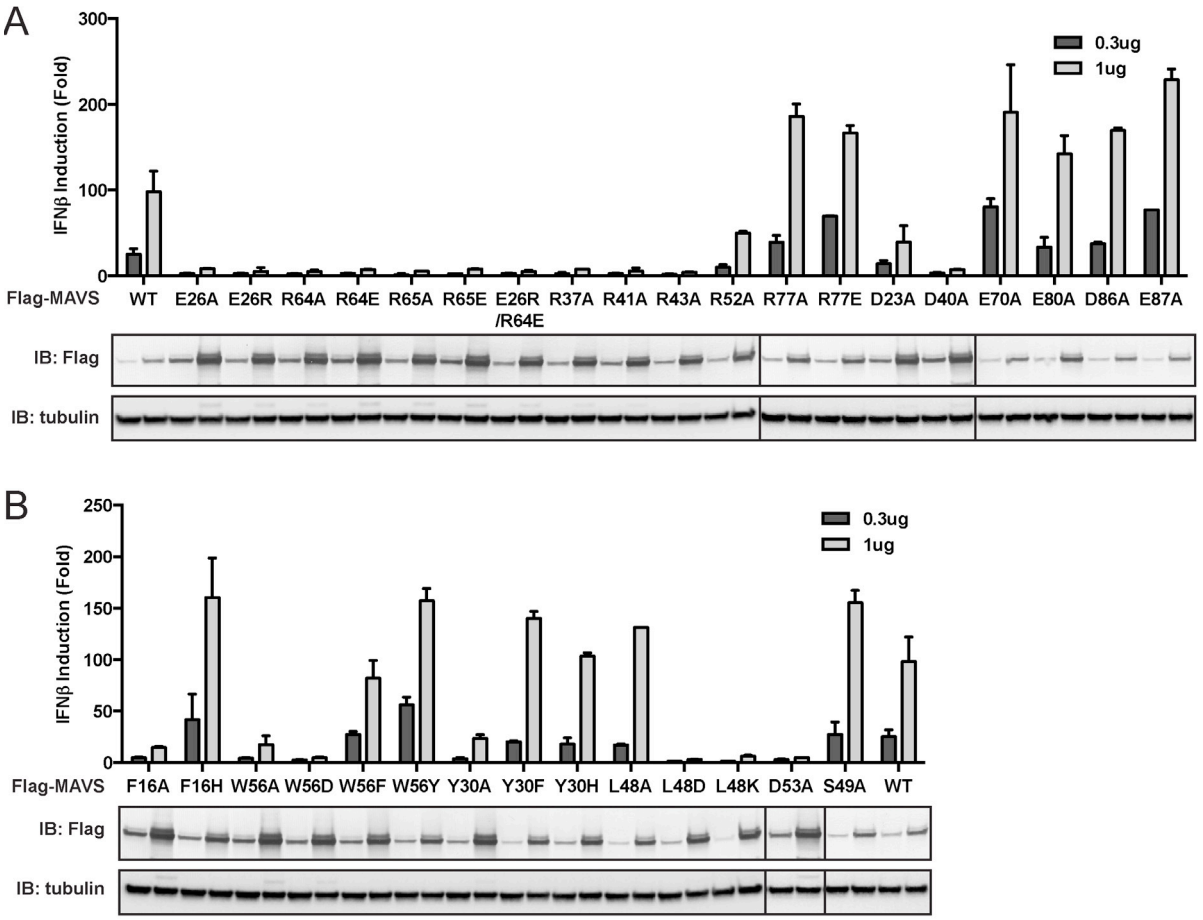

Figure 16 Signaling activity of wild-type MAVS and mutants.
(A)(B) Wild-type MAVS and CARD mutants were transiently expressed in HEK293T-IFNβ-luciferase reporter cells. Cells were lysed 24 hr later, and the induced IFNβ was measured by luciferase assay. Western blot was done to monitor the expression level of the transfected MAVS with α-tubulin as the loading control.

interface is R52, whose replacement by alanine significantly decreased its activity (Figure 16B).

At interface III, the hydrophobic core formed by L48 of each MAVS CARD monomer is important for the filament formation (Figure 15A, top view). Although L48 is not conserved among all the species, substitution of L48 with charged residues (D or K), but not alanine, completely abolished MAVS activity in HEK293T cells (Figure 16B). The hydrophobicity and small side chain of A44 may be important for the packing at this interface because mutating A44 to T impaired MAVS CARD filament formation *in vitro* (Table 4). In addition to the hydrophobic patch close to the central pore of the filament, the electrostatic interactions mediated by residues R37, R41, D40 and D53 at the outer rim of the filament are also important. Single alanine substitution of these residues almost completely abolished MAVS activity (Figures 16A and B).

To test the specificity of the electrostatic interactions at the MAVS CARD assembly interfaces, we mutated several charged residues outside the interfaces and assessed their effects on MAVS activity. E70 and R77 in H5, E80 in the loop between H5 and H6, and D86 and E87 in H6 are outside the interfaces (Figure 15F). Their substitution with alanine or reversely charged residues still allowed potent induction of IFNβ production in HEK293T cells (Figure 16A).

Structure-based mutagenesis *in vitro*

To further test whether these mutations impaired the MAVS signaling activity because they interfered with CARD polymerization, CARD mutants were purified from *Escherichia*

coli and their oligomerization states were examined. Unlike wild-type MAVS CARD, which eluted in the void volume in gel filtration chromatography, mutants with impaired MAVS signaling activity eluted as monomers (E26R as an example in Figure 17A; Table 4). EM images of the negatively stained proteins (E26R as an example in Figure 17B) verified that these mutations impaired the filament formation of MAVS CARD. These results indicate that mutations that abrogate interactions at the interfaces prevent MAVS CARD oligomerization and abolish MAVS activity.

We also collaborated with Dr. Xiaojing He in Dr. Xuewu Zhang lab to obtain the crystal structures of several MAVS CARD mutants, which were monomeric in solution. Well diffracting crystals were obtained for horse MAVS CARD soluble mutants but not for the human proteins. Those mutants adopt almost exactly the same structure as the wild-type protein (e.g., Figure 17C for the horse E26R and R64C structures; Table 4). This suggested that these mutations did not disrupt the filament by changing the structural fold of each subunit, but instead by altering the interface chemistry.

Probing the oligomerization interfaces of MAVS by a solubility screen

As an alternative verification of the key residues for MAVS CARD self-association, we searched for mutants that disrupt the CARD polymerization in *E. coli* (Table 4). Random mutagenesis and the screen for soluble MAVS CARD mutants by a recently developed solubility screen (Harada et al., 2008) were performed by Dr. Xiaojing He. Mutated CARDs fused to murine dihydrofolate reductase (mDHFR) were expressed. While mDHFR fused to wild-type CARD appeared in inclusion bodies due to CARD oligomerization, it remained

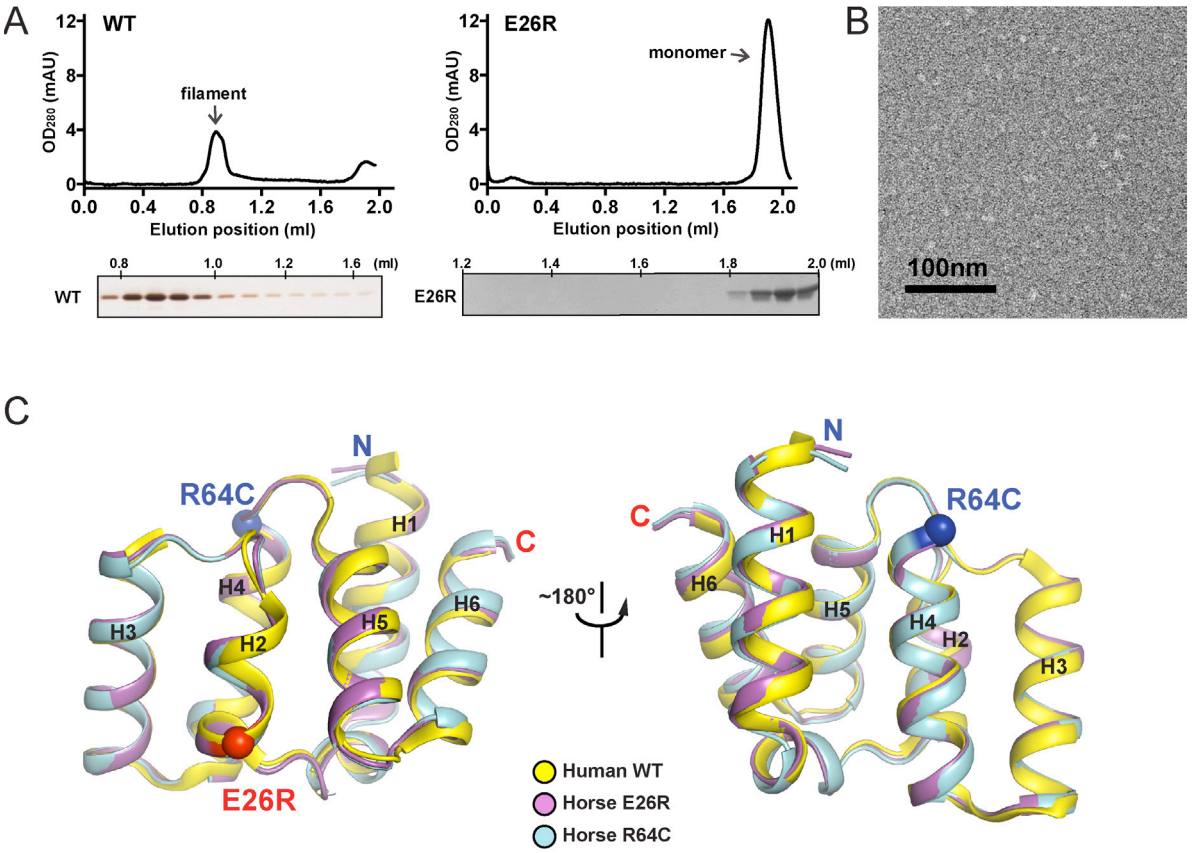

Figure 17 Mutations at the interfaces disrupt MAVS CARD polymerization.
(A) Size-exclusion chromatography of recombinant wild-type human MAVS CARD and the E26R mutant. Aliquots of the fractions were analyzed by silver staining (left) or Coomassie Blue staining (right). Wild-type MAVS CARD eluted in the void volume (~0.8 ml), while the soluble mutant E26R eluted at ~1.9 ml.
(B) Negative stain EM image of human MAVS CARD E26R mutant. No filaments were observed. Scale bar, 100 nm.
(C) Superimposition of the crystal structures of wild-type human MAVS CARD (PDB: 2VGQ, yellow) with horse MAVS CARD E26R (PDB: 4O9L, magenta) and R64C mutants (PDB: 4O9F, blue). The Cα atoms of E26R and R64C in the crystal structures are shown in sphere representation (red and blue, respectively).

Table 4 Summary of MAVS CARD mutants

	Human				Horse			
Residues	Mutants	Screen	Solubility	Activity	Mutants	Screen	Solubility	Crystal
F16	F16A			P				
	F16H			Y				
	F16I	✓	++					
D23	D23A			P				
	D23N	✓						
E26	E26A		++	N				
	E26R		+++	N	E26R		++	✓
	E26R/ R64E			N				
Y30	Y30A			P				
	Y30F			Y				
	Y30H			Y				
	Y30C	✓	+					
R37	R37A			N				
	R37K	✓						
D40	D40A			N				
R41	R41A			N				
R43	R43A			N				
A44	A44D	✓						
	A44T		++		A44T	✓	++	✓
L48	L48A			Y				
	L48D			N				
	L48K			N				
R52	R52A			P				
D53	D53A			N				
W56	W56A		++	P				
	W56D			N				
	W56F			Y				
	W56Y			Y				
	W56E		+++					
	W56R	✓	++					
R64	R64A			N				
	R64E		+++	N				
	R64Q	✓	++					
	R64C		++		R64C	✓	+++	✓
					R64S	✓	+++	✓
R65	R65A			N				
	R65E			N				
	R65Q	✓						
					R65S	✓	++	
					R65H	✓		

Note:

1. Solubility is based on the estimated final yield of the purified protein per liter of bacterial culture. +++: >5mg/L; ++: 1-5mg/L; +: <1mg/L.
2. Activity was tested as in Figure 16: N, no activity; P, partial activity; Y, no defect in activity;
3. Solubility screen and crystallization were performed by Dr. Xiaojing He.

soluble when it was fused to a CARD mutant that failed to oligomerize. Expression of soluble mDHFR-CARD was selected by trimethoprim, which specifically inhibits bacterial DHFR, but not mDHFR. The screen recognized multiple sites that are important for CARD oligomerization (Table 4). Biochemical analysis confirmed that most mutants from the screen were expressed as soluble proteins, and eluted as homogenous monomers in gel filtration chromatography (E26R as an example in Figure 17A).

All the mutations out of the solubility screen can be mapped to the three types of interfaces identified in the C1 model (Figure 15). A44, an important residue revealed by the solubility screen, is located at interface III of the C1 model but not at the two types of interfaces based on the C3 model. The loss-of-function mutation, A44T, may disrupt the hydrophobic patch at interface III of the C1 model, but it is difficult to be explained by the C3 model.

CARD serves as the organization center for MAVS filaments

Previously we have shown that a deletion mutant of MAVS (MAVSΔProTM; Figure 7A) lacking part of the proline-rich region (PRR, residues 103-153) and the C-terminal transmembrane domain (TM; residues 461-540) allowed the production of a large amount of protein from *E. coli*, and remained capable of inducing wild-type MAVS to form fibers that potently induced IRF3 dimerization in cytosolic extracts (Hou et al., 2011). Compared to

full-length MAVS, MAVSΔProTM is soluble when fused with SUMO, and can form functional polymers after removal of SUMO. Because MAVSΔProTM resembles the soluble part of MAVS, its filament structure probably closely represents the polymerization of endogenous MAVS on mitochondria.

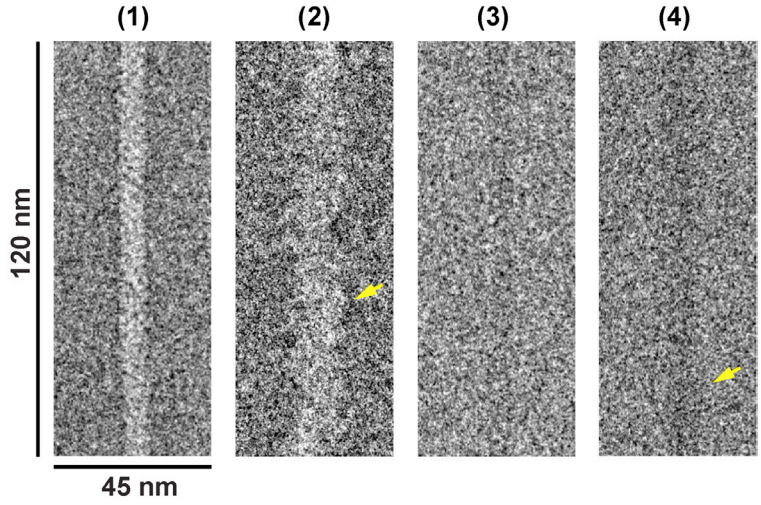

Figure 18 Segments from negative stain EM images of (1) Flag-MAVS CARD and (2) MAVSΔProTM and those from cryoEM images of (3) Flag-MAVS CARD and (4) MAVSΔProTM. Yellow arrows point to the extra mass that made MAVSΔProTM filaments larger in diameter.

When we compared the EM images of MAVSΔProTM filaments with those of MAVS CARD filaments, the former apparently had extra mass and were larger in diameter than the latter (Figure 18). We built a cryoEM dataset of 10,903 boxed segments out of individual MAVSΔProTM filaments. The averaged power spectrum of overlapping filament segments and power spectra of 2D class averages exhibited a similar pattern of layer lines as the CARD filaments. This suggests that the core of MAVSΔProTM filament takes the same left-handed helical structure as the CARD only filament.

The segment between the CARD and the TM domain of MAVS is intrinsically disordered as predicted by protein secondary and ternary structure prediction software. As the CARD filament is in the center of MAVS aggregates, the rest of the molecule is connected to the peripheral surface of the filament. In the case of full-length MAVS aggregates at the surface of mitochondria, the C-terminal TM domain is integrated in the mitochondrial membrane so the CARD filament and the membrane anchor the two ends of each MAVS molecule. This may facilitate the intervening region to be exposed and to recruit cytosolic signaling effector molecules such as the TRAF (tumor necrosis factor receptor-associated factor) proteins (Liu et al., 2013).

CARD is crucial for the MAVS filament formation in cells

To visualize the filament formation of full-length MAVS, we stably reconstituted Mavs-null murine embryonic fibroblasts (MEFs) with Flag-tagged wild-type MAVS or its mutants. Although transient expression of wild-type MAVS resulted in constitutive signaling (Kawai et al., 2005; Meylan et al., 2005; Seth et al., 2005; Xu et al., 2005), the low expression level in the stable cell lines did not lead to constitutive activation of downstream target genes. Like endogenous protein, Flag-tagged MAVS was properly localized to the mitochondrial membranes, as demonstrated by its co-localization with either MitoTracker or TOM20, a 20 kDa subunit of the translocase in the mitochondrial outer membrane (Figures 19 and 20A, Mock). Infection by Sendai virus induced the redistribution of MAVS and the formation of densely packed, speckled MAVS puncta on the surface of mitochondria, along with the nuclear translocation of NF-κB subunit p65 and induction of interferon-β (IFNβ)

(Figure 20A). The formation of MAVS aggregates induced by Sendai virus infection was also detected by semi-denaturing detergent agarose electrophoresis (SDD-AGE) (Figure 21A; Hou et al., 2011). Based on the nuclear translocation of p65 after viral infection, these bright MAVS puncta were observed in a majority of virus-infected cells (Figure 21B). In contrast, the bright puncta did not form in cells expressing MAVS mutants that failed to form filaments (Figures 20A and B). As negative controls, mutants (E80A and F16H) that do not affect the MAVS filament formation were found to have normal puncta formation (Figures

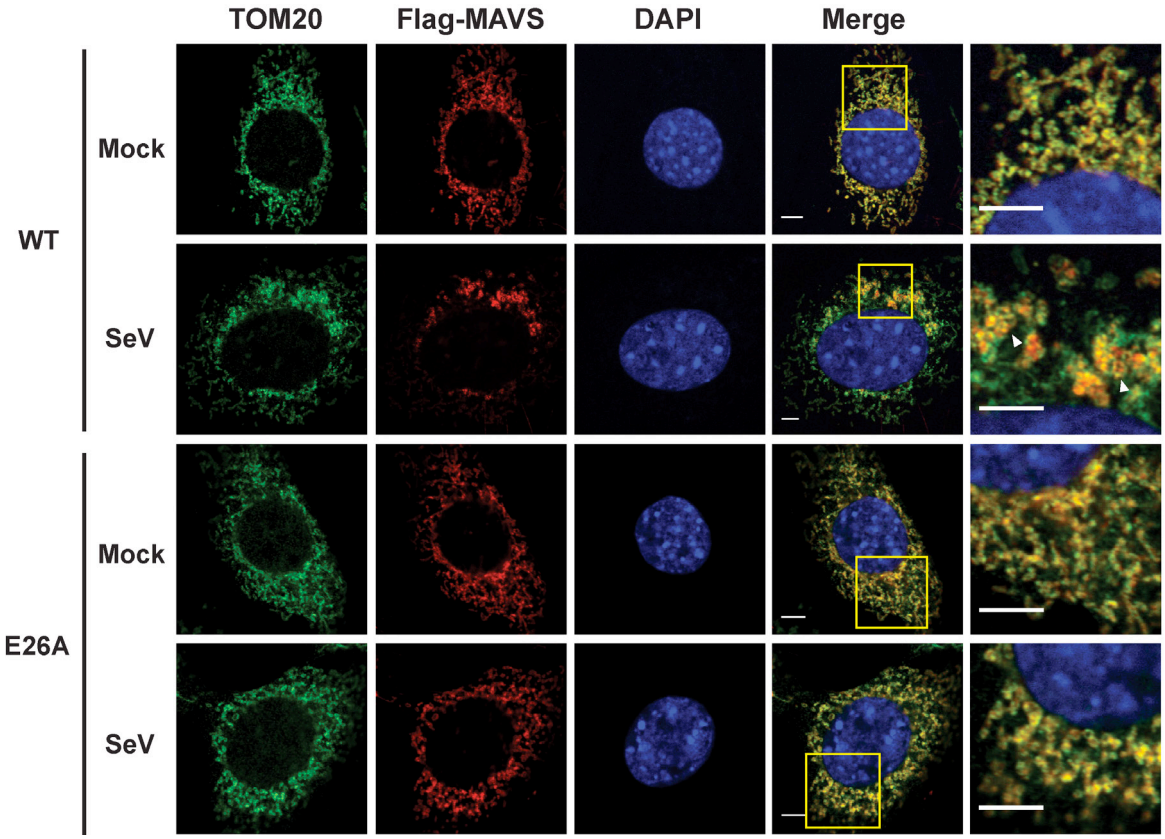

Figure 19 MAVS puncta formation and redistribution were examined using confocal microscopy.
Mitochondria were stained by TOM20 antibody (mitochondrial outer membrane). Areas within the yellow windows in the merged images are expanded and shown in the rightmost images. MAVS puncta are highlighted by white arrowheads. Scale bars, 5.0 μm.

20A and B). These results support that the CARD-mediated aggregate formation is the key structural element for activating MAVS signaling in cells (Figures 21A and C).

Because the confocal fluorescent images of MAVS aggregates did not have enough resolution to reveal the shape of the puncta in virus-infected cells, we next performed the experiments using Super Resolution Structured Illumination Microscopy (SR-SIM) (Gustafsson et al., 2008). The resolution of conventional fluorescence microscopy is limited to ~200 nm in lateral (x, y) dimensions, and ~500 nm along the optical axis. SR-SIM

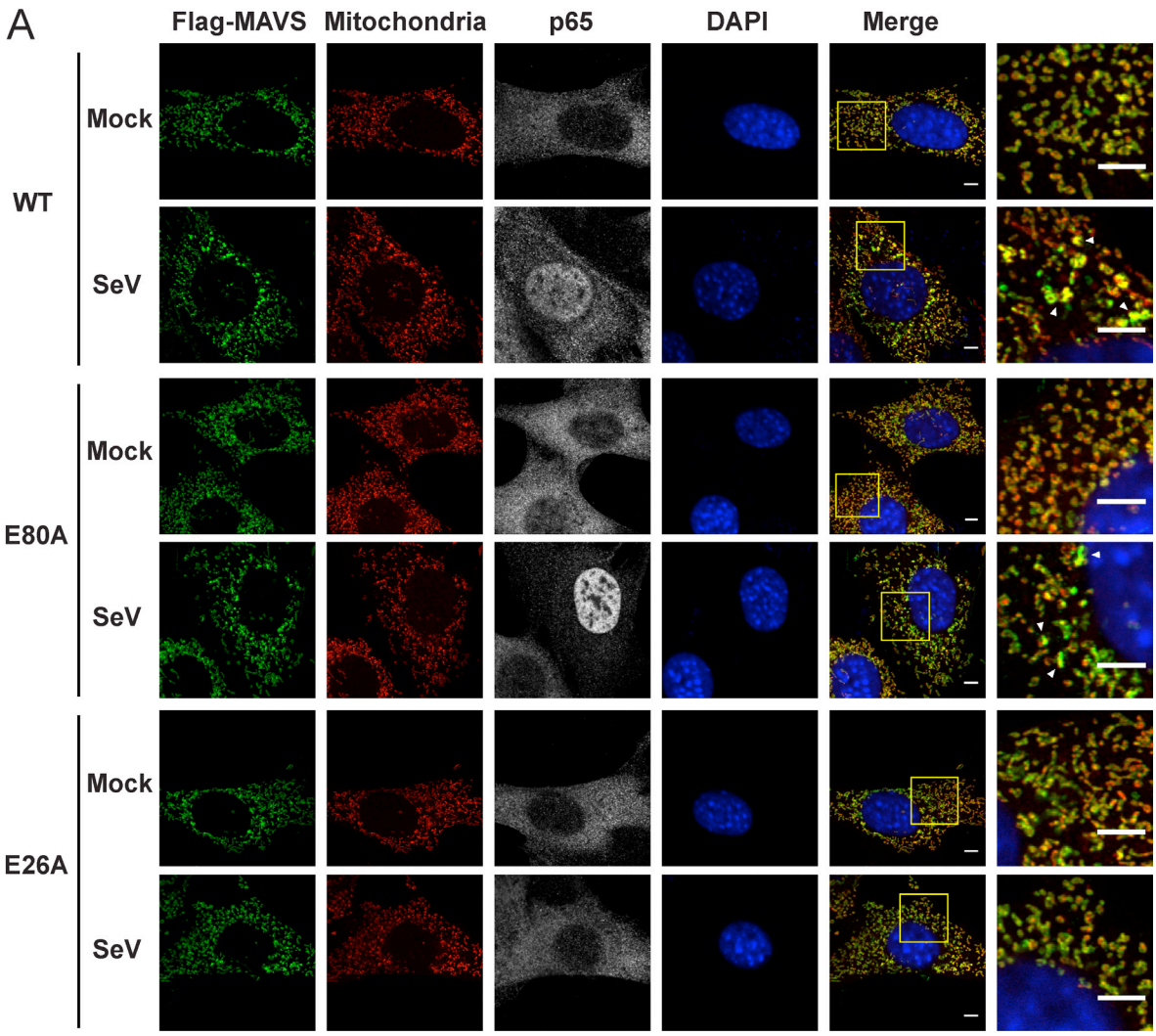

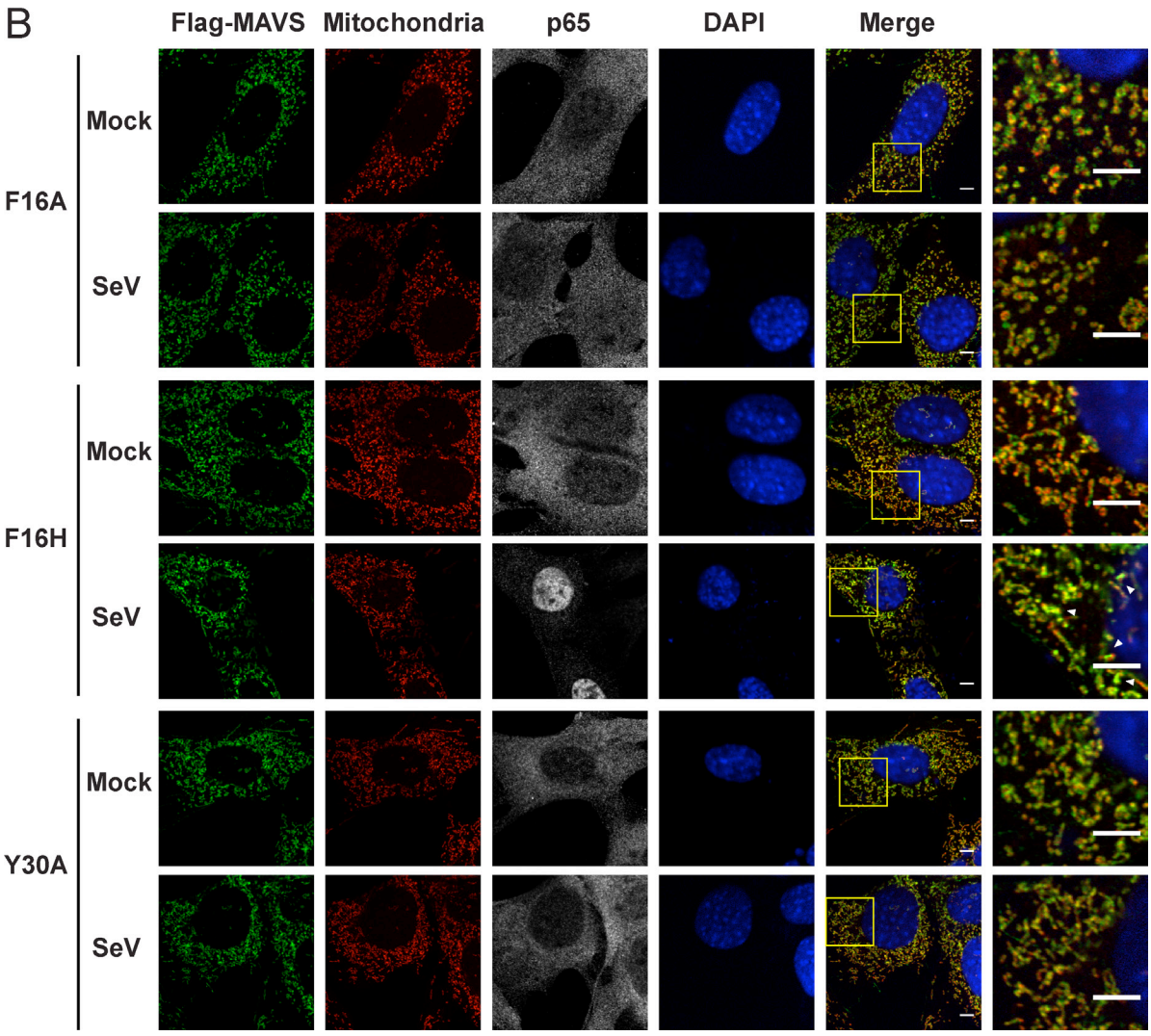

Figure 20 Mutations at the interfaces that disrupt CARD polymerization abolish the SeV-induced redistribution of MAVS on mitochondria.
Mavs$^{-/-}$ MEF cells stably expressing Flag-tagged wild-type MAVS or its mutants were mock-treated or infected with SeV for 12 hr and stained with MitoTracker (Mitochondrial matrix; red), anti-Flag antibody (Flag-MAVS; green), anti-p65 antibody (grey) and DAPI (blue). MAVS redistribution was examined using confocal microscopy. Areas within the yellow windows in the merged images are expanded and shown in the rightmost images. MAVS puncta are highlighted by white arrowheads. WT, E80A in (A) and F16H in (B) showed strong puncta formation and clear p65 nuclear translocation, whereas mutations at the interfaces, E26A in (A), F16A and Y30A in (B) did not. E80 is a conserved charged residue as a control. Scale bars, 5.0 μm.

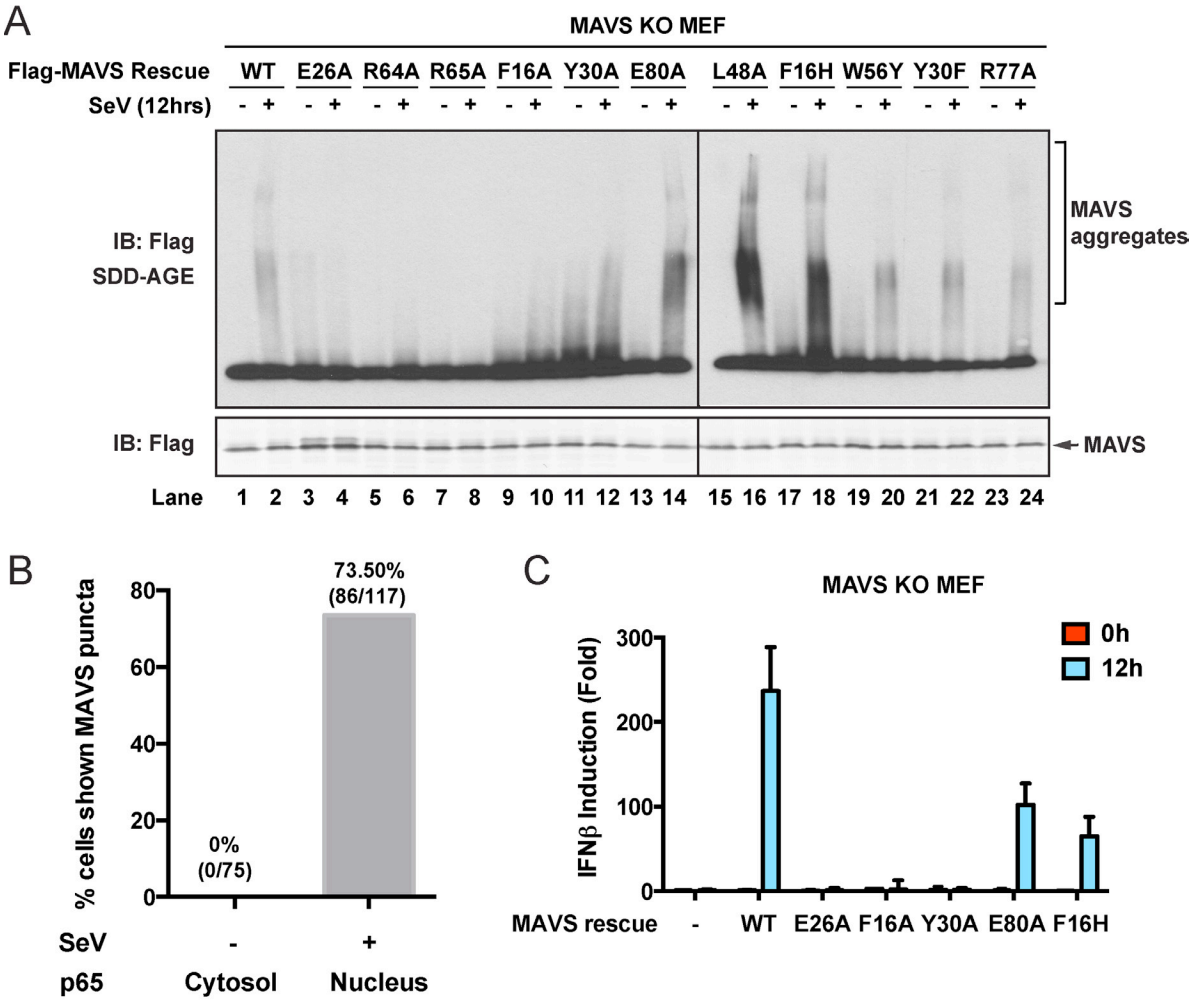

Figure 21 Strong correlations among MAVS puncta formation, MAVS signaling and MAVS CARD polymerization.

Mavs$^{-/-}$ MEF cells stably expressing Flag-tagged wild-type MAVS or its mutants were mock-treated or infected with SeV for 12 hr.

(A) MAVS proteins in the mitochondrial extracts from different cells were separated by SDD-AGE (top) or SDS-PAGE (bottom) followed by western blotting. Cells expressing wild-type MAVS and mutants (E80A, L48A, F16H, W56Y, Y30F and R77A) that rescued IFNβ production gave rise to strong aggregation signal in the SDD-AGE assay, whereas MAVS mutants defective in forming puncta or inducing IFNβ (E26A, R64A, R65A, F16A and Y30A) did not form aggregates. Y30A showed slightly higher basal aggregation signal, independent of viral infection.

(B) Statistical analysis of the correlation between nuclear translocation of p65 and SeV-induced MAVS puncta formation in Mavs$^{-/-}$ MEF cells expressing wild-type MAVS. No p65 nuclear translocation was observed in uninfected cells. Among cells showing clear p65

translocation, only those showing large MAVS puncta (> 0.4 μm) were classified as positive. Even with such strict constraints, more than 70% of the cells were positive.
(C) IFNβ production was rescued by expressing MAVS wild-type and mutants (E80A and F16H) that retain the capability of forming MAVS puncta, but not those (E26A, F16A and Y30A) that failed to form puncta (Figures 19 and 20). The IFNβ mRNA level was quantified by q-RT-PCR.

increases both the lateral and axial resolutions by a factor of two (Gustafsson et al., 2008). SR-SIM images of Flag-tagged wild-type MAVS showed a fairly uniform distribution on the surface of mitochondria as it appeared in concentric rings around almost every MitoTracker-stained mitochondrion (Figure 22A, the last image in the top row). In cells infected with Sendai virus, the SR-SIM images revealed a clear redistribution of MAVS into rod-shaped clusters that interfaced with only a small fraction of mitochondria (e.g., white arrowheads in the rightmost image of the bottom row in Figure 22A). Because there was no obvious difference in the expression level of MAVS in these cells before and after viral infection (Figure 21A; Hou et al., 2011; Liu et al., 2013), the redistribution of MAVS from one mitochondrion to another during the puncta formation may result from mitochondrial fusion and fission dynamics (Yasukawa et al., 2009; Castanier et al., 2010; Koshiba et al., 2011). The diameter of the rod-shaped MAVS clusters is probably less than 100 nm, the lateral resolution limit of SR-SIM.

When a series of SR-SIM images were combined in IMARIS to reconstruct a 3D volume of MAVS and mitochondria in virus-infected cells (Figure 22B), it became clear that the MAVS aggregates were not evenly distributed around individual mitochondria, but were clustered into narrow regions on the surface of mitochondria (the rightmost image in Figure 22B). Many of these rod-shaped clusters bridge between two or more mitochondrial

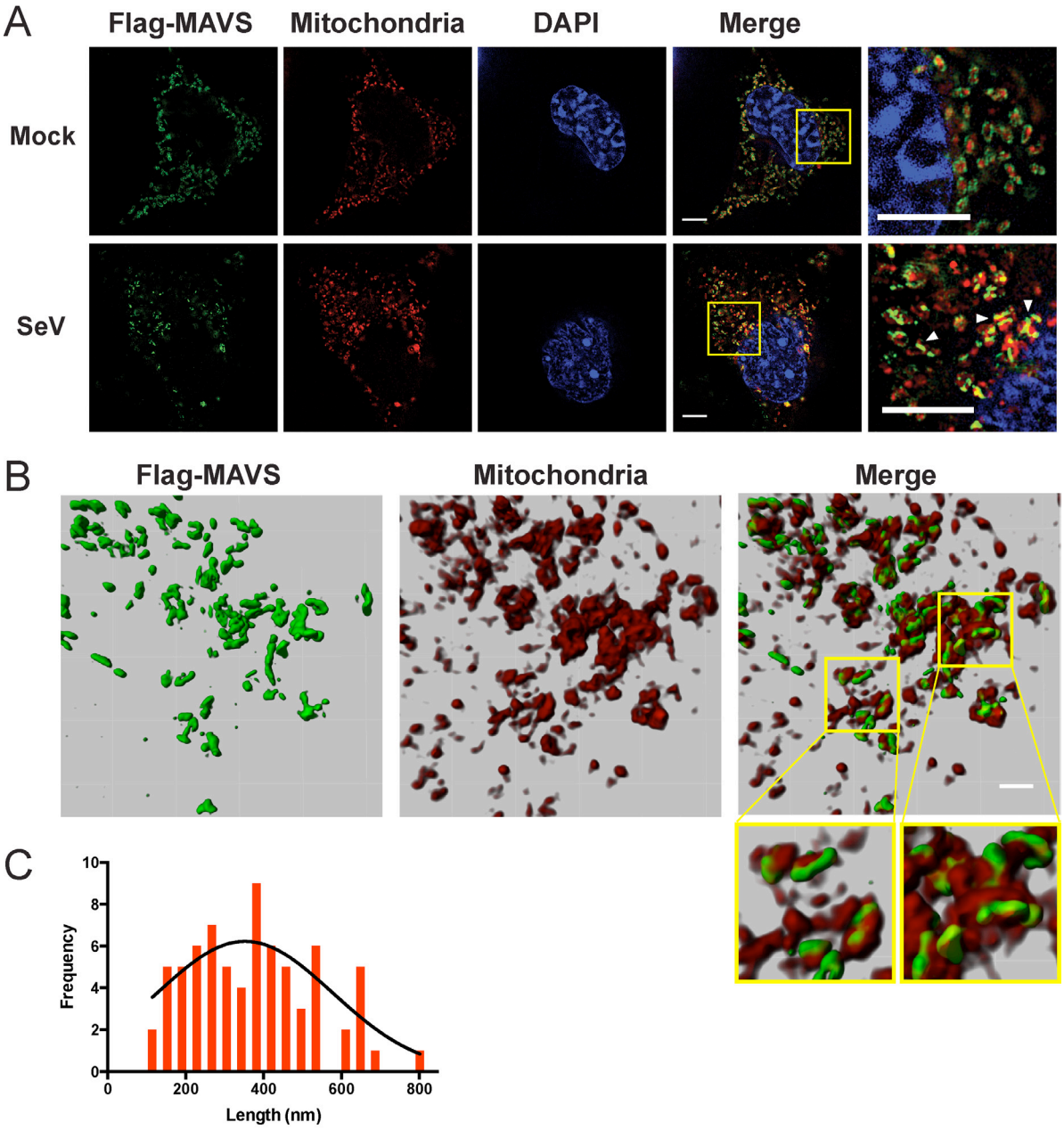

Figure 22 In virus-infected cells MAVS redistributes and forms rod-shaped puncta on the surface of mitochondria.

(A) Mavs$^{-/-}$ MEF cells stably expressing Flag-tagged wild-type MAVS were mock-treated or infected with Sendai virus (SeV) for 12 hr and stained with MitoTracker (Mitochondria; red) and anti-Flag antibody (Flag-MAVS; green). Redistribution of MAVS among mitochondria was examined using SR-SIM. Expanded views of the areas within the yellow windows in the merged images were shown on the right. The SeV-infected cells contain bright foci of Flag-

MAVS. The white arrowheads in the rightmost image of the bottom row highlight a few bright rod-shaped MAVS clusters. Scale bars, 5.0 μm.
(B) 3D reconstruction of MAVS clusters (green) on the surface of mitochondria (red). Scale bar, 1.0 μm. The areas within the yellow windows in the merged image (rightmost) were expanded to show a few clusters that appear to bridge between mitochondrial membranes.
(C) Histogram and Gaussian fit (black curve) of the length distribution of individual MAVS clusters (N = 74) in virus-infected cells measured from SIM images.

membranes, suggesting that MAVS molecules from multiple mitochondria may contribute to the formation of one MAVS filament (magnified insets of Figure 22B). To quantify the average number of MAVS molecules for the rod-shaped clusters, we measured the length distribution of many observed clusters in the 2D SR-SIM images (Figures 22A and C). The mean filament length in the observed Poisson distribution is approximately 400 nm (full width at half maximum, or FWHM, n = 74) and the longer ones are ~800 nm. Based on the cryoEM map, each 400 nm filament contains approximately 790 MAVS molecules.

In vitro reconstitution of the activation of full-length MAVS by MAVS CARD filaments

To study the activation of full-length MAVS *in vitro*, I first tried to purify full-length MAVS in an inactive state from HEK293T cells stably expressing Flag-MAVS (Figure 23A). Since overexpression led to MAVS aggregation that constitutively activated downstream target genes (Hou et al., 2011), cell lines with low expression level were selected. Analysis of the mitochondrial extracts using sucrose gradient ultracentrifugation showed that although a small fraction of Flag-MAVS formed aggregates in the absence of viral infection (Figure 23B, top), the vast majority of MAVS formed the active complex in a manner dependent on Sendai virus infection (Figure 23B, bottom). Unlike MAVS CARD and MAVSΔProTM

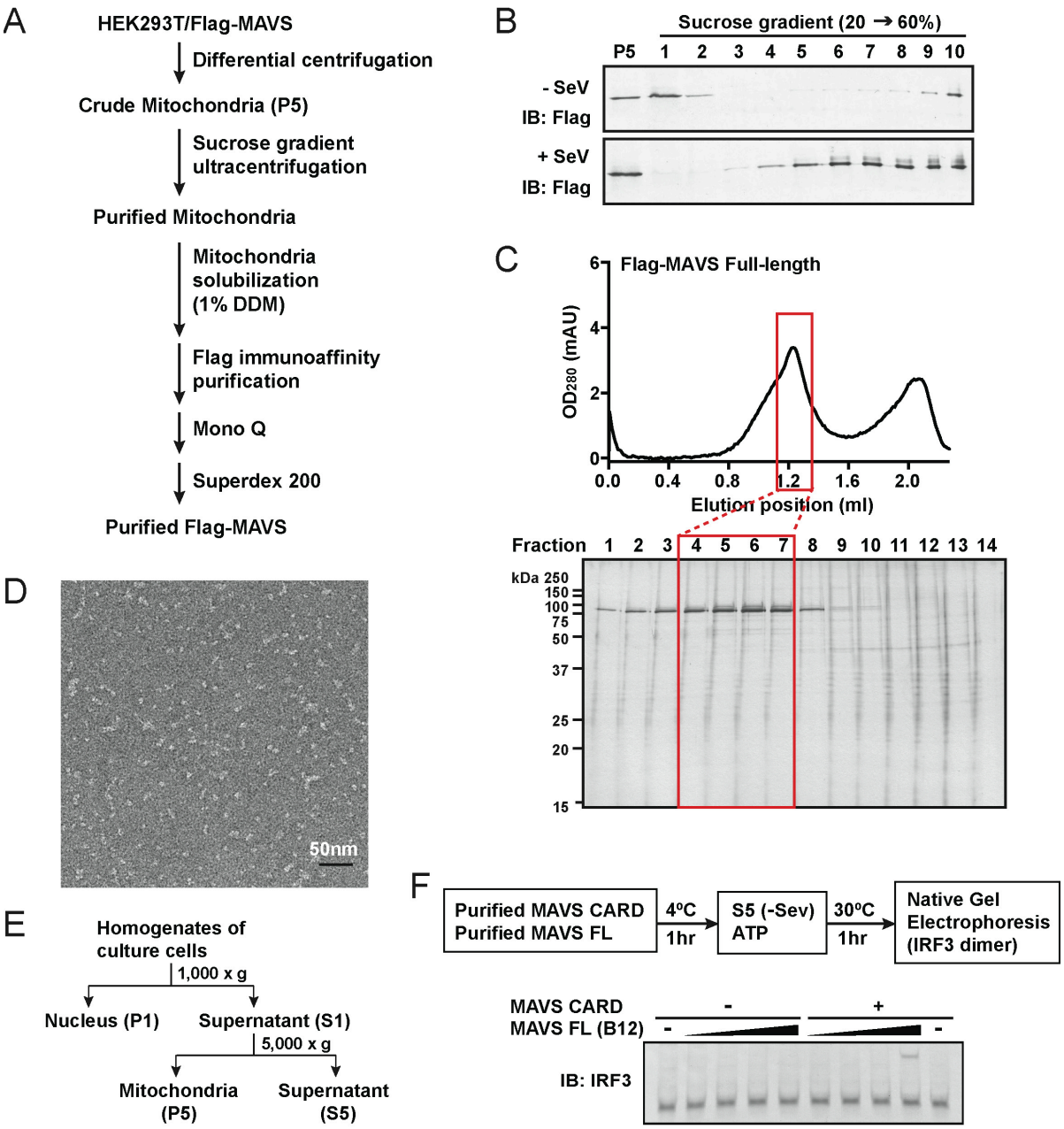

Figure 23 Purification and *in vitro* reconstitution of the activation of full-length MAVS.
(A) Procedures for purification of full-length Flag-MAVS.
(B) Crude mitochondria isolated from HEK293T-Flag-MAVS stable cells infected with Sendai virus for 12 hr (+SeV) or uninfected (-SeV) were solubilized in a buffer containing 1% DDM and then subjected to sucrose gradient ultracentrifugation. The fractions were analyzed by MAVS immunoblotting.

(C) Size-exclusion chromatography of full-length Flag-MAVS. Aliquots of the fractions were analyzed by silver staining. Unlike MAVS CARD filaments, which eluted in the void volume (~0.8 ml), full-length MAVS eluted at ~1.25 ml.
(D) Negative stain EM image of purified full-length MAVS. No filaments were observed. Scale bar, 50 nm.
(E) Procedures for isolation of crude mitochondria (P5) and cytosolic extracts (S5) by differential centrifugation.
(F) *In vitro* activation of full-length MAVS by MAVS CARD filaments. Purified full-length MAVS was incubated with purified MAVS CARD filaments. After incubation, aliquots of the reaction mixtures were further incubated with cytosolic extracts (S5) from uninfected HEK293T cells in the presence of ATP, and then IRF3 dimerization was analyzed by native gel electrophoresis.

filaments, which eluted in the void volume in gel filtration chromatography, full-length MAVS eluted in later fractions corresponding to the elution volume of a soluble globular protein of approximately 160 kDa (Figure 23C). The purified MAVS did not spontaneous form filaments as shown in negative stain EM images (Figure 23D).

The activity of purified MAVS was tested by a cell-free assay containing downstream target genes in the cytosol of uninfected cells. Cytosolic extracts (S5) were separated from crude mitochondria (P5) from HEK293T cells by differential centrifugation (Figure 23E). The formation of IRF3 dimer, which is a hallmark of IRF3 activation, was measured by native gel electrophoresis. *In vitro* incubation of the purified full-length MAVS with cytocolic extracts (S5) did not cause IRF3 dimerization, suggesting that the purified protein was in an inactive state. The purified full-length MAVS gained the ability to activate IRF3 after incubating with MAVS CARD filaments, although MAVS CARD filaments alone did not activate IRF3 (Figure 23F). This suggested that the purified full-length MAVS was functional and capable of being activated. The *in vitro* reconstitution of the induced activation of full-length MAVS by MAVS CARD filaments further suggested that MAVS

activation occurred through a prion-like mechanism, which was triggered and templated by the N-terminal CARD domain. This activity assay can be further used to dissect the activation mechanism of MAVS by RIG-I/RNA/Ub complex and other regulators.

CHAPTER THREE
DISCUSSION

The RIG-I/MAVS antiviral pathway plays a critical role in host defense against virus infection. The recently reported crystal structures of RIG-I in RNA free and bound forms significantly extend our understanding of the domain rearrangement of RIG-I upon RNA binding. However, it was not clear why the ATPase activity of RIG-I is essential for its activation and what is the role of the ATP-driven translocation of RIG-I on dsRNA. Using *in vitro*-transcribed RNAs of different lengths as model ligands, I showed that RIG-I oligomerized on 5'ppp dsRNA in an ATP hydrolysis-dependent and dsRNA length-dependent manner, which correlated with the strength of type-I interferon (IFN-I) activation. The negative stain EM structure of full-length RIG-I in complex with a 5'ppp stem-loop RNA and ATP, together with the crystal structure of RIG-I/ubiquitin complex, suggested a two-step oligomerization of RIG-I for activation.

Based on other studies and the data presented here, we propose a structure-based model of RIG-I activation (Figure 24). RIG-I first forms a small binding unit upon recognition of 5'ppp dsRNA, which is independent of ATP binding. This triggers a conformation change of RIG-I to expose the N-terminal tandem CARDs. ATP hydrolysis then drives the translocation of RIG-I on dsRNA, which allows exposure of 5'ppp and recruitment of additional RIG-I molecules on dsRNA, facilitating the formation of a dsRNA length-dependent oligomer of RIG-I. K63-linked polyubiquitin chains then interact with the exposed CARDs from adjacent RIG-I to form RIG-I tetramers that further activate MAVS to induce type-I interferon production.

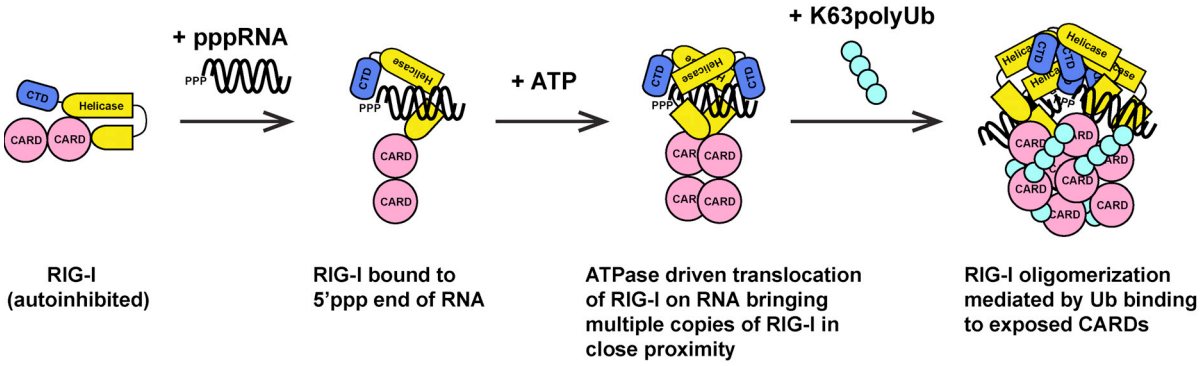

Figure 24 A proposed model of RIG-I activation.

Our high-resolution data showed that MAVS CARD assembled into left-handed filaments with C1 symmetry. The pseudoatomic model of MAVS CARD filament suggests that after viral infection activated MAVS molecules on the mitochondrial surface interact with each other through three types of interfaces between CARD domains (Figure 25). The MAVS aggregates in cells are indeed rod-shaped clusters that may contain MAVS molecules from multiple mitochondria. The CARD filaments form the central elements of MAVS aggregates, and can promote their own growth by attracting new CARDs into the pre-poised interaction interfaces. The filaments are localized on the mitochondrial surface and the MAVS TM domains are embedded inside the mitochondrial outer membranes. These two ends of each MAVS molecule provide important spatial constraints that may force the intervening coiled sequence to be well extended and exposed for recruiting down-stream signaling molecules (Liu et al., 2013; Figure 25). Bioinformatic analysis suggests that the middle segment of MAVS forms random coils, which, if present by themselves in aqueous phase, would not likely be fully extended and thus may deter efficient binding of multiple positive or negative regulators of MAVS. The spatial arrangement between the CARD

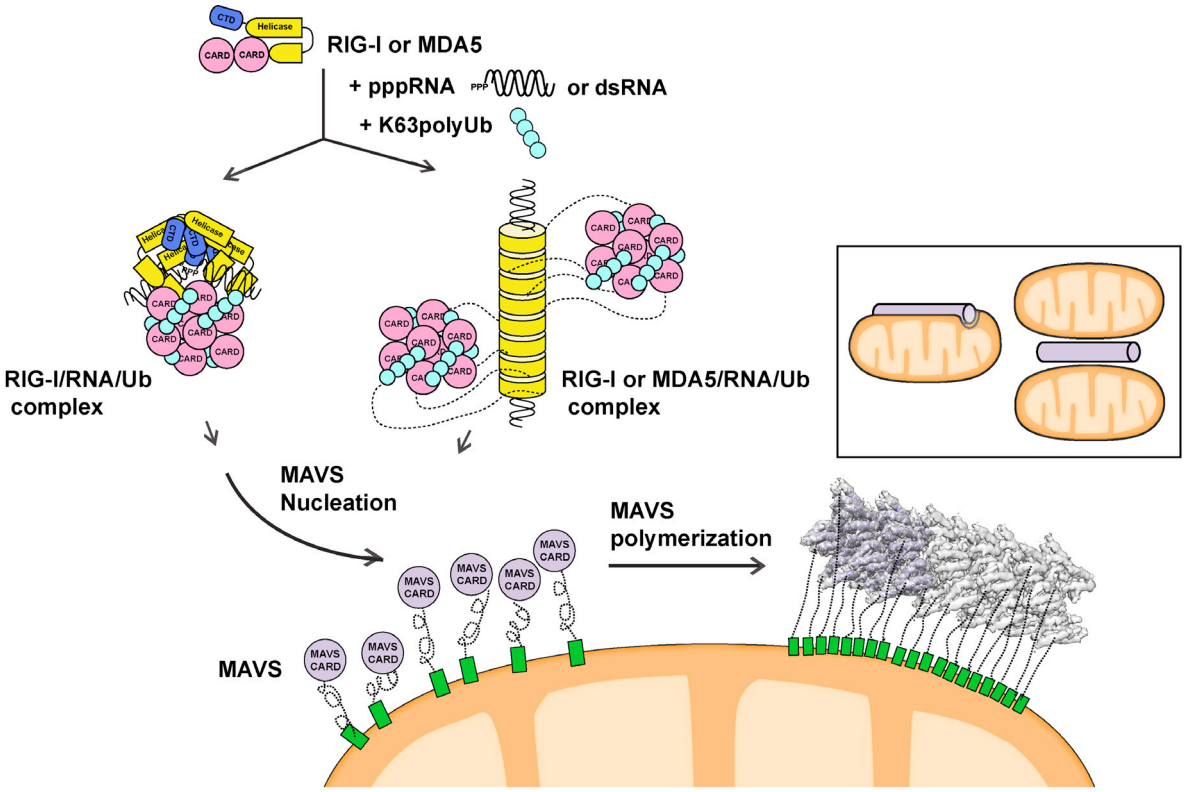

Figure 25 A proposed model for MAVS activation by RLRs.
Detection of 5'pppRNA by RIG-I or dsRNA by RIG-I or MDA5 triggers the formation of RIG-I (or MDA5)/RNA/polyUb complex. The CARD domains of RIG-I in the complex are poised properly to attract MAVS CARDs and support the nucleation of the filament. In the resting state, MAVS CARD is sequestered and has a low probability of forming polymers. The RIG-I (or MDA5)/RNA/polyUb complex stabilizes MAVS CARDs in the exposed state and initiate the filament formation. Once started, a short MAVS CARD filament promotes its own elongation by attracting more MAVS CARDs into the assembly. The filament can form on the surface of one mitochondrion or between two or more mitochondrial membranes. Inset, one or more mitochondria might be involved in MAVS filament formation.

filament and the mitochondrial membrane provides a good solution to this problem of intrinsic disorder. The prion-like filament formation of MAVS thus uses very different chemistry than other prion proteins, and orchestrates the signaling domains of MAVS into a high-affinity platform for rapid and efficient signaling.

The filament formation of MAVS CARD is based on collective interactions at the six interfaces of each subunit according to the C1 map (Figures 15). These interfaces maintain the tight and dense packing of individual CARDs in the filaments, which, together with the strong electrostatic interactions, probably make the filaments detergent-resistant. During filament formation, there are counter-acting forces, such as decrease in entropy, which would increase the energy level of the filaments. The net decrease in free energy supporting the filament formation is due to the six interaction interfaces for every CARD. But the counter-balance of these positive and negative energy terms likely makes the filaments fairly sensitive to mutations. Indeed, the six interfaces appear to be dominated by hot spots because point mutations in multiple positions are capable of destabilizing the filaments. The filament grows with time and long filaments about several microns long were observed under cryoEM conditions. Inside virus-infected cells, the average length of the rod-shaped MAVS clusters is merely ~400 nm. The physical length of MAVS filaments in cells may be limited by the number of MAVS molecules in each mitochondrion and by the dynamics of mitochondrial fusion and fission (Onoguchi et al., 2010; Figure 22C).

The prion-like polymerization of MAVS CARD causes MAVS redistribution on the surface of mitochondria and the possible bridging of multiple mitochondria by the MAVS filaments (Figure 22B). The limited number of MAVS molecules per mitochondrion suggests that the long MAVS filaments may be contributed by multiple mitochondria. The clustered MAVS molecules become sequestered during the dynamic mitochondrial fusion and fission cycles. The fusion of sequestered clusters leads to the redistribution of MAVS from being ubiquitously present in almost all mitochondria to being segregated on a small number of

them. The self-promoting nature of MAVS filaments may be the driving force that leads to almost all MAVS being incorporated into filaments (Figures 20A and 22A). Further analyses of MAVS redistribution and its correlation with mitochondrial fusion/fission dynamics by live-cell imaging and computational analysis may provide more detailed insights into this process.

Protein oligomerization mediated by the death domain (DD) superfamily, which is composed of the Death Domain (DD), Caspase Activation and Recruitment Domain (CARD), Death Effector Domain (DED) and Pyrin Domain (PYD) subfamilies, has been studied in multiple signaling proteins (Ferrao and Wu, 2012). For example, the helical assembly of MyDDosome was proposed to use three different types of DD-DD interfaces (Lin et al., 2010; Gay et al., 2011; Kersse et al., 2011). The MyDDosome formation is to bring multiple kinase domains of the IRAKs together for efficient activation. This affinity-enhancing scheme for recruiting downstream effectors may be a common feature for proteins in the DD superfamily. The prion-like polymerization of MAVS filaments would thus entail a significant amplification of the signal and enhance the sensitivity of the RLR-mediated antiviral signaling. Because TRAF2 and TRAF3 both form trimers (Park et al., 1999; Ni et al., 2000; Zheng et al., 2010; Napetschnig and Wu, 2013), MAVS filaments may enhance the TRAF-MAVS interaction through increased avidity, and boost the signaling efficacy significantly.

In summary, our structural and functional studies of the RIG-I/RNA interaction, RIG-I/ubiquitin interaction and MAVS polymerization revealed a highly sensitive and efficient signaling cascade for viral RNA sensing to trigger a rapid innate immune response. Such

digital (i.e., all or none) response allows the organisms to defend against noxious agents such as lethal infections.

CHAPTER FOUR
METHODS

Reagents and standard methods

Mouse antibody against Flag-tag (M2) and M2-conjugated agarose were purchased from Sigma-Aldrich (St. Louis, MO); rabbit antibodies against TOM20 and the p65 subunit of NF-κB were from Santa Cruz Biotechnology (Dallas, TX); Alexa Fluor 488 conjugated goat anti-mouse and anti-rabbit antibodies, Alexa Fluor 568 conjugated goat anti-mouse antibody, and Alexa Fluor 633 conjugated goat anti-rabbit antibody were from Invitrogen (Carlsbad, CA). Sendai virus (SeV, Cantell strain, Charles River Laboratories) was used at 100 hemagglutination (HA) units/ml culture media. HEK293T, HEK293T-IFNβ-luciferase, $Mavs^{-/-}$ MEF cells and derivatives were cultured in Dulbecco's modified Eagle's medium (DMEM) supplemented with 10% (v/v) cosmic calf serum (Hyclone, Thermo Fisher Scientific, Waltham, MA) with penicillin (100 U/ml) and streptomycin (100 μg/ml). Other chemicals and reagents were from Sigma-Aldrich unless otherwise specified.

RNA *in vitro* transcription and purification

DNA templates containing the T7 promoter (5' TAATACGACTCACTATAG 3') were used for *in vitro* transcription reactions using a homemade T7 RNA polymerase. Large-scale transcription reactions were carried out at 37°C for 2-4 h, followed by digestion at 37°C for 30 min with Turbo DNaseI (Ambion Inc.) for removal of DNA templates. The resulting products were purified using phenol-chloroform extraction and ethanol precipitation. The

RNAs were separated in denaturing urea polyacrylamide gels (15-20%) and the desired bands were excised for RNA extraction.

RIG-I expression and purification

cDNA encoding full-length human RIG-I (residues 2-925) was cloned into the N-terminal His_6-tagged Gateway™ baculovirus expression vector pDEST10 (Invitrogen) with a TEV protease cleavage site inserted after His-tag. The resulting vector was used to transform DH10Bac (Invitrogen) cells for generating recombinant bacmid DNAs. The bacmids were used to transfect SF9 cells and high-titer virus stocks were generated by several rounds of amplification. Cells were harvested 72 hours after infection and lysed by sonication. The protein was purified using affinity, ion exchange and gel filtration chromatography to apparent homogeneity. Gel filtration analysis showed that RIG-I eluted as a single symmetrical peak with an expected molecular mass of ~110 kDa, indicating that it is a monomer. In the presence of 22bp 5'ppp bpLRNA and ATP, RIG-I formed two types of complex as detected by native gel. The dimeric and monomeric RIG-I complexes were separated by gel filtration.

K63-linked ubiquitin chain synthesis and purification

Methods for synthesizing K63-linked polyUb chains were described previously (Pickart and Raasi, 2005). Briefly, K63-linked polyUb chains with specific lengths were synthesized stepwise by adding one ubiquitin in the reaction at a time. The ubiquitination reactions contained E1, Ubc13, Mms2 and two ubiquitin mutants K63R and D77. Reaction

was stopped with 5 mM EDTA and reduced with 5 mM DTT at room temperature for 15 min. The synthesized ubiquitin chains were then purified using HiTrap SP HP column (GE Healthcare). Ubiquitin C-terminal hydrolase (UCH) was used in reaction to remove D77 followed by HiTrap Q HP column (GE Healthcare) purification.

MAVS expression and purification

cDNA encoding Flag-tagged MAVS CARD (1-100) has been described previously (Hou et al., 2011). For MAVS CARD expression, pcDNA3-Flag-MAVS CARD was transiently transfected into HEK293T cells. Cells were harvested 36 hr after transfection and lysed in a buffer containing 20 mM Tris-HCl (pH 8.0), 150 mM NaCl, 10% glycerol, 0.1% Triton X-100, 1 mM DTT, and EDTA-free protease inhibitor cocktail (Roche, Basel, Switzerland). After centrifugation at 10,000×g for 10 min, Flag-MAVS CARD was selectively bound to anti-Flag (M2) agarose beads and eluted by Flag peptide. The eluate was fractionated on a Superdex 200 PC 3.2/30 column (GE Healthcare, Uppsala, Sweden) equilibrated in a buffer containing 20 mM Tris-HCl (pH 7.5), 50 mM NaCl and 1 mM DTT. Fractions were analyzed by SDS-PAGE and silver staining.

cDNA encoding the MAVSΔProTM mutant lacking the proline-rich region (103-153) and the C-terminal transmembrane domain (461-540) has been described previously (Hou et al., 2011). The bacterial expression vector pET28a-His_6-SUMO-MAVSΔProTM was transformed into BL21 (pLys). Protein expression was induced with 0.2 mM IPTG at 18°C for four hours. After sonication in a lysis buffer containing 10 mM Tris-HCl (pH 8.0), 500 mM NaCl, 0.5 mM DTT, 5% glycerol, 0.5 mM PMSF and 10 mM imidazole, cell lysates

were centrifuged at 50,000×g for 30 min. His_6-SUMO-MAVSΔProTM in the supernatant was purified using Ni-NTA affinity resin (QIAGEN, Limburg, Netherlands). Subsequently, the protein was loaded onto HiTrap Q HP column (GE Healthcare), and then eluted with a gradient of NaCl varying from 0.1 M to 0.5 M in a buffer made of 10 mM Tris-HCl (pH 7.5), 5% glycerol, 2 mM DTT, 1 mM EDTA and 0.5 mM PMSF. The fractions containing His_6-SUMO-MAVSΔProTM, which were eluted with 300 mM NaCl, were pooled together and applied to a Superdex 200 HR 10/30 column (GE Healthcare) equilibrated with a buffer made of 10 mM Tris-HCl (pH 8.0), 150 mM NaCl, 1 mM DTT, 1 mM EDTA and 0.5 mM PMSF. His_6-SUMO-MAVSΔProTM was then digested with SUMO protease at 4°C overnight. The His_6-SUMO tag was removed by running the reaction mixture in a Superdex 200 PC 3.2/30 column (GE Healthcare), which was equilibrated in a buffer containing 10 mM Tris-HCl (pH 8.0), 150 mM NaCl and 1 mM DTT. The peak fraction was collected for EM studies.

Procedures to purify functional full-length MAVS from uninfected cells were described in Figure 23A. HEK293T cells stably expressing Flag-MAVS (human) were lysed in a buffer containing 10 mM Tris-HCl (pH 8.0), 10 mM KCl, 0.25 M D-mannitol, 1mM DTT, 0.5mM PMSF, 1mM EDTA, 0.5mM EGTA and protease inhibitors by repeated douncing. After differential centrifugation, pellet was washed once with homogenization buffer. Crude mitochondria were resuspended and loaded on top of a centrifuge tube containing 4.5 ml of 50% sucrose on the bottom layer and 4.5 ml of 35% sucrose on the top layer. After centrifugation at 60,000xg for 20 min, mitochondria enriched at the interface of two layers were collected and solubilized in a buffer containing 20 mM Tris-HCl (pH 8.0),

200 mM NaCl, 10% glycerol, 1% DDM, 1mM DTT, 1mM PMSF, 1mM EDTA, 0.5mM EGTA and protease inhibitors at 4°C for 2hr. After centrifugation at 10,000xg for 10min, the supernatant was incubated with anti-Flag (M2) agarose beads, followed by elution of Flag-MAVS with Flag peptide. The eluate was loaded onto Mono Q column (GE Healthcare), and then eluted with a gradient of NaCl varying from 0.1 M to 0.5 M in a buffer made of 20 mM Tris-HCl (pH 7.5), 5% glycerol, 0.05% DDM, 1 mM DTT and 0.5 mM PMSF. The fractions containing Flag-MAVS, which were eluted with 150 mM NaCl, were pooled together and applied to a Superdex 200 PC 3.2/30 column (GE Healthcare) equilibrated in a buffer containing 20 mM Tris-HCl (pH 7.5), 150mM NaCl, 5% glycerol, 0.05% DDM and 1 mM DTT. Fractions were analyzed by SDS-PAGE and silver staining. The peak fraction was collected for EM studies and activity assay.

Negative stain electron microscopy

Copper grids (Ted Pella Inc., Redding, CA) coated with a thin layer (3-5 nm) of carbon were rendered hydrophilic by negative glow discharge in air. A 2-4 µl aliquot of the purified sample was loaded onto the grids. After 30 s of incubation on the grid at room temperature, the sample was stained with 2.0% phosphotungstic acid (PTA) at pH 8.0 and blotted dry. Samples were imaged in a JEOL 2200FS FEG electron microscope operated at 200 kV. Images of the RIG-I/RNA complex were recorded on SO163 films (Eastman Kodak, Rochester, NY) with a nominal magnification of 60,000 × under low-dose conditions (~20 $e^{-}/Å^{2}$) using a defocus range of −1.0 to −2.0 µm. Films were developed using full-strength D19 (Kodak) solution and selected on a SIRA optical diffractometer. Good micrographs

were digitized with a PhotoScan film Scanner (Z/I Imaging GmbH, Germany) at a step size of 14.0 μm. All particles were picked interactively using BOXER (EMAN) and processed using IMAGIC and SPIDER. MAVS CARD and MAVSΔProTM filaments were imaged with a nominal magnification of 50,000 × (2.84 Å/pixel at the detector level) using a defocus range of −0.7 to −1.5 μm. Images were recorded with an electron dose of ~20 $e^{-}/Å^2$ on a 2K × 2K Tietz slowscan Charge Coupled Device (CCD) camera. Full-length MAVS was imaged with a nominal magnification of 25,000 × using a defocus range of −1.0 to −2.0 μm on a Gatan K2 Summit Direct Detector (Gatan, Pleasanton, CA).

CryoEM sample preparation and data collection

Quantifoil R2/2 grids (Quantifoil Micro Tools GmbH, Jena, Germany) were coated with a thin layer of carbon in order to retain more filaments for imaging. Right before use, the grids were negatively glow-discharged in air. 2.5 μl purified MAVS was loaded onto the grids. Grids were blotted in 100% humidity at 4°C for 5-8 s before being plunge-frozen into liquid ethane bathed in liquid nitrogen inside a Vitrobot (FEI, Hillsboro, OR). There are altogether 6 datasets of MAVS CARD filaments collected using different microscopes, detectors and at different magnifications (Table 2). Datasets 1-3 were collected using JEOL 2200FS FEG electron microscope and recorded on SO163 films with a nominal magnification of 60,000 × or 50,000 × under low-dose conditions (~20 $e^{-}/Å^2$). A total of 358 films were developed and micrographs were digitized at a step size of 7.0 μm. After 2 × 2 binning, the pixel size for dataset 1 was 2.33 Å on the specimen. Datasets 4-5 were collected at HHMI Janelia Farm Research Campus using an FEI Titan Krios microscope with a Falcon

I direct electron detector. Dataset 6 was collected using an FEI Titan Krios with a Falcon II direct electron detector. The microscope was operated at 300 kV and was equipped with a Cs corrector. Automatic data collection was run by proprietary software, EPU (FEI, Hillsboro, OR). Images were taken under −2.5 to −4.0 μm of defocus.

CryoEM image processing of MAVS filaments

Quality of cryoEM images was evaluated by Fourier transforms. Contrast transfer function parameters were estimated using CTFFIND3 (Mindell and Grigorieff, 2003). Filament segments were manually boxed from good images using EMAN2 helixboxer (Ludtke et al., 1999). Selected filaments were segmented using individual boxes that had 90% overlap between neighboring ones (Table 2). We used a customized version of Relion (Scheres et al., 2012, Clemens et al., 2015) developed by Dr. Peng Ge in Dr. Z. Hong Zhou lab at UCLA for 2D and 3D classifications and refinements. This 'helical' Relion contains an implementation of the IHRSR method based on the framework of Relion 1.2. Two maps with C1 or C3 symmetry were filtered to 30 Å as reference models for 3D classifications. The structures were refined with the autorefine function of Relion until convergence. The resolution was estimated by the gold-standard scheme in Relion as well as using EMAN proc3d.

The C1 map calculated from dataset 6 was obtained by Dr. Peng Ge. The other data processing in ‘helical’ Relion presented here was performed by me. Data processing of datasets 1-4 and parallel sorting of C1 and C3 symmetries using SPIDER were performed by Dr. Qiu-Xing Jiang.

Cryo-electron tomography (cryo-ET)

Energy-filtered electron cryo-tomography on the MAVS CARD filaments was carried out from a dataset collected with an FEI Titan Krios at HHMI Janelia Farm Research Campus. The tomography tilt series were collected in a Gatan K2 Summit direct electron detector installed behind a GIF Quantum energy filter. A narrow energy slit of 5 eV was used together with a small objective aperture (50 microns) to enhance image contrast. The data were collected at a nominal magnification of 42,000 ×, corresponding to 2.7 Å/pixel on the K2 camera. The tilt range spans from −60 to +60° with a step size of 3°. The defocus level was set at −6.0 microns. Tomographic reconstruction was carried out using the standard weighted back projection procedure implemented in IMOD (Yu et al., 2013). The tilt series were aligned using patch tracking due to the absence of fiducial gold particles. A non-linear anisotropic diffusion filter was applied to the reconstruction. For better resolution of the helical stripes, five slices that cover the top surfaces of multiple filaments in the tomogram were used to calculate a projection image (Figure 10), and the view was from above the filaments. The angle between the stripes and the helical axis and the distance between stripes were measured in the image.

Interferon-β luciferase reporter assay

HEK293T cells stably expressing both Renilla luciferase (as an internal control) and IFNβ promoter driving firefly luciferase were transfected with the indicated amounts of cDNAs for Flag-tagged wide-type MAVS or its mutants. 24 hr after transfection, cells were

harvested to measure the expression of luciferase using a dual luciferase assay kit (Promega, Madison, WI).

Confocal and SR-SIM imaging

$Mavs^{-/-}$ MEFs stably expressing wide-type MAVS or its mutants were grown on sterile glass coverslips in 12-well plates. 12 hr after Sendai virus infection, cells were first stained with MitoTracker Red according to the manufacturer's instructions (Invitrogen). Cells were then fixed with 4.0% paraformaldehyde in PBS for 15 min, permeabilized in PBS containing 0.1% Triton X-100 for 5 min, and blocked in PBS containing 0.1% Triton X-100 and 10% BSA for 30 min at room temperature. After blocking, cells were incubated with specific primary antibodies for 1 hr, washed and then incubated with suitable Alexa Fluor 488 (or Alexa Fluor 568 or Alexa Fluor 633)-conjugated secondary antibodies for another hour. After careful wash, slides were mounted with the VECTASHIELD mounting medium with DAPI (Vector Laboratories). Imaging of the cells was carried out using a Zeiss LSM510 META laser scanning Confocal Microscope or a Zeiss ELYRA PS.1 Super-Resolution Structured Illumination Microscope (SR-SIM). Z-stacks with an interval of 110 nm were used to section the whole cell for 3D-SR-SIM. Images were analyzed using the Zen2011 software (Zeiss) or ImageJ. Alignment and reconstruction of 3D-SIM images were performed using IMARIS (Bitplane).

Quantitative reverse transcription PCR (q-RT-PCR)

Total RNA was isolated using TRIzol (Invitrogen). 0.1 μg of total RNA was reverse-transcribed into cDNA with iScript cDNA synthesis kit (Bio-Rad, Hercules, CA). The resulting cDNAs served as the templates for Quantitative-PCR analysis using iTaq Universal SYBR Green Supermix (Bio-Rad) and ViiTM7 Real-Time PCR System (Applied Biosystems Inc., Foster City, CA). Primers for specific genes are: Mouse β-actin, 5′-TGACGTTGACATCCGTAAAGACC-3′ and 5′-AAGGGTGTAAAACGCAGCTCA-3′; Mouse IFNβ, 5′-CCCTATGGAGATGACGGAGA-3′ and 5′-CTGTCTGCTGGTGGAGTTCA-3′.

Semi-denaturing detergent agarose gel electrophoresis (SDD-AGE)

The formation of prion-like aggregates of MAVS and its mutants was analyzed by SDD-AGE as described (Hou et al., 2011).

In vitro IRF3 dimerization assay

Crude mitochondria (P5) and cytosolic extracts (S5) were prepared by differential centrifugation as described (Zeng et al., 2009). In brief, HEK293T cells were resuspended in a buffer containing 10 mM Tris-HCl (pH 7.5), 10 mM KCl, 1.5 mM $MgCl_2$, 0.25 M D-mannitol and EDTA-free protease inhibitor cocktail (Roche) and then lysed by repeated douncing. Cell homogenates were centrifuged at 1,000xg for 5 min to pellet nuclei. Postnuclear supernatant was further centrifuged at 5,000xg for 10 min to separate mitochondria (P5) from cytosolic supernatant (S5). Purified MAVS proteins were incubated

at 4°C for 1 hr and then incubated with S5 and ATP at 30°C for 1hr. IRF3 dimerization was analyzed by native gel electrophoresis as described (Zeng et al., 2010).

BIBLIOGRAPHY

Adams PD, Grosse-Kunstleve RW, Hung LW, Ioerger TR, McCoy AJ, Moriarty NW, Read RJ, Sacchettini JC, Sauter NK, Terwilliger TC. 2002. PHENIX: building new software for automated crystallographic structure determination. Acta Crystallographica Section D Biological Crystallography 58:1948–1954.

Bai XC, Fernandez IS, McMullan G, Scheres SH. 2013. Ribosome structures to near-atomic resolution from thirty thousand cryo-EM particles. eLife 2, e00461.

Baum A, Sachidanandam R, Garcıa-Sastre A. 2010. Preference of RIG-I for short viral RNA molecules in infected cells revealed by next-generation sequencing. Proc. Natl. Acad. Sci. USA 107:16303–8

Berke IC, Modis Y. 2012. MDA5 cooperatively forms dimers and ATP-sensitive filaments upon binding double-stranded RNA. The EMBO Journal 31:1714–1726.

Binder M, Eberle F, Seitz S, Mucke N, Huber CM, Kiani N, Kaderali L, Lohmann V, Dalpke A, Bartenschlager R. 2011. Molecular mechanism of signal perception and integration by the innate immune sensor retinoic acid inducible gene-I (RIG-I). J Biol Chem 286: 27278–27287.

Cai X, Chen J, Xu H, Liu S, Jiang Q X, Halfmann R, Chen ZJ. 2014. Prion-like polymerization underlies signal transduction in antiviral immune defense and inflammasome activation. Cell 156, 1207-1222.

Castanier C, Garcin D, Vazquez A, Arnoult D. 2010. Mitochondrial dynamics regulate the RIG-I-like receptor antiviral pathway. EMBO Reports 11:133–138.

Civril F, Bennett M, Moldt M, Deimling T, Witte G, Schiesser S, Carell T, Hopfner KP. 2011. The RIG-I ATPase domain structure reveals insights into ATP-dependent antiviral signalling. EMBO Reports 12:1127–1134.

Clemens DL, Ge P, Lee BY, Horwitz MA, Zhou ZH. 2015. Atomic Structure of T6SS Reveals Interlaced Array Essential to Function. Cell 160, 940-951.

Cui S, Eisenacher K, Kirchhofer A, Brzozka K, Lammens A, Lammens K, Fujita T, Conzelmann KK, Krug A, Hopfner KP. 2008. The C-terminal regulatory domain is the RNA 5'-triphosphate sensor of RIG-I. Molecular cell *29*, 169-179.

Egelman, EH. 2007. Single-particle reconstruction from EM images of helical filaments. Current opinion in structural biology *17*, 556-561.

Egelman EH. 2007. The iterative helical real space reconstruction method: surmounting

the problems posed by real polymers. Journal of Structural Biology 157:83–94.

Egelman EH. 2010. Reconstruction of helical filaments and tubes. Methods in enzymology 482, 167-183.

Egelman, EH. 2014. Ambiguities in helical reconstruction. eLife *3*.

Emsley P, Cowtan K. 2004. Coot: model-building tools for molecular graphics. Acta Crystallographica Section D Biological Crystallography 60:2126–2132.

Emsley P, Lohkamp B, Scott WG, Cowtan K. 2010. Features and development of Coot. Acta Crystallographica Section D Biological Crystallography 66:486–501.

Fairman-Williams ME, Guenther UP, Jankowsky E. 2010. SF1 and SF2 helicases: family matters. Current Opinion in Structural Biology 20:313–324.

Frank J. 2006. Three-dimensional electron microscopy of macromolecular assemblies. New York: Oxford University Press. 2nd edition.

Ferrao R, Wu H. 2012. Helical assembly in the death domain (DD) superfamily. Current opinion in structural biology 22, 241-247.

Fujita T. 2009. A nonself RNA pattern: tri-p to panhandle. Immunity 31:4–5.

Gack MU, Shin YC, Joo CH, Urano T, Liang C, Sun L, Takeuchi O, Akira S, Chen Z, Inoue S, Jung JU. 2007. TRIM25 RING-finger E3 ubiquitin ligase is essential for RIG-I-mediated antiviral activity. Nature 446, 916-920.

Gay NJ, Gangloff M, O'Neill LA. 2011. What the Myddosome structure tells us about the initiation of innate immunity. Trends in immunology 32:104–109.

Gustafsson MG, Shao L, Carlton PM, Wang CJ, Golubovskaya IN, Cande WZ, Agard DA, Sedat JW. 2008. Three-dimensional resolution doubling in wide-field fluorescence microscopy by structured illumination. Biophysical Journal 94:4957–4970.

Harada BT, Knight MJ, Imai S, Qiao F, Ramachander R, Sawaya MR, Gingery M, Sakane F, Bowie JU. 2008. Regulation of enzyme localization by polymerization: polymer formation by the SAM domain of diacylglycerol kinase delta1. Structure 16:380–387.

He H, Yang T, Terman JR, Zhang X. 2009. Crystal structure of the plexin A3 intracellular region reveals an autoinhibited conformation through active site sequestration. Proceedings of the National Academy of Sciences of the United States of America 106:15610–15615.

Hild N, Schneider OD, Mohn D, Luechinger NA, Koehler FM, Hofmann S, Vetsch JR, Thimm BW, Muller R, Stark WJ. 2011. Two-layer membranes of calcium phosphate/collagen/PLGA nanofibres: in vitro biomineralisation and osteogenic differentiation of human mesenchymal stem cells. Nanoscale 3:401–409.

Hornung V, Ellegast J, Kim S, Brzozka K, Jung A, Kato H, Poeck H, Akira S, Conzelmann KK, Schlee M, Endres S, Hartmann G. 2006. 5'-Triphosphate RNA is the ligand for RIG-I. Science 314:994–997.

Hou F, Sun L, Zheng H, Skaug B, Jiang QX, Chen ZJ. 2011. MAVS forms functional prion-like aggregates to activate and propagate antiviral innate immune response. Cell 146:448–461.

Iwasaki A, Medzhitov R. 2010. Regulation of adaptive immunity by the innate immune system. Science 327:291–295.

Iwasaki K. 2012. Electron microscopic imaging of integrin. Methods in Molecular Biology 757:111–128.

Jiang F, Ramanathan A, Miller MT, Tang GQ, Gale M, Patel SS, Marcotrigiano J. 2011. Structural basis of RNA recognition and activation by innate immune receptor RIG-I. Nature 479:423–427.

Jiang X, Kinch LN, Brautigam CA, Chen X, Du F, Grishin NV, Chen ZJ. 2012. Ubiquitin-induced oligomerization of the RNA sensors RIG-I and MDA5 activates antiviral innate immune response. Immunity 36:959–973.

Kato H, Takeuchi O, Sato S, Yoneyama M, Yamamoto M, Matsui K, Uematsu S, Jung A, Kawai T, Ishii KJ, et al. 2006. Differential roles of MDA5 and RIG-I helicases in the recognition of RNA viruses. Nature 441, 101-105.

Kato H, Takeuchi O, Mikamo-Satoh E, Hirai R, Kawai T, Matsushita K, Hiiragi A, Dermody TS, Fujita T, Akira S. 2008. Length-dependent recognition of double-stranded ribonucleic acids by retinoic acid-inducible gene-I and melanoma differentiation-associated gene 5. The Journal of Experimental Medicine 205:1601–1610.

Kawai T, Akira S. 2006. Role of IPS-1 in type I IFN induction. Nihon Rinsho Japanese Journal of Clinical Medicine 64:1231–1235.

Kawai T, Takahashi K, Sato S, Coban C, Kumar H, Kato H, Ishii KJ, Takeuchi O, Akira S. 2005. IPS-1, an adaptor triggering RIG-I- and Mda5-mediated type I interferon induction. Nature Immunology 6:981–988.

Kersse K, Verspurten J, Vanden Berghe T, Vandenabeele P. 2011. The death-fold superfamily of homotypic interaction motifs. Trends in Biochemical Sciences 36:541–552.

Kohlway A, Luo D, Rawling DC, Ding SC, Pyle AM. 2013. Defining the functional determinants for RNA surveillance by RIG-I. EMBO Reports 14:772–779.

Kolakofsky D, Kowalinski E, Cusack S. 2012. A structure-based model of RIG-I activation. RNA *18*, 2118-2127.

Koshiba T, Yasukawa K, Yanagi Y, Kawabata S. 2011. Mitochondrial membrane potential is required for MAVS- mediated antiviral signaling. Science signaling 4:ra7.

Kowalinski E, Lunardi T, McCarthy AA, Louber J, Brunel J, Grigorov B, Gerlier D, Cusack S. 2011. Structural basis for the activation of innate immune pattern-recognition receptor RIG-I by viral RNA. Cell 147:423–435.

Lee MH, Lalwani P, Raftery MJ, Matthaei M, Lutteke N, Kirsanovs S, Binder M, Ulrich RG, Giese T, Wolff T, Krüger DH, Schönrich G. 2011. RNA helicase retinoic acid-inducible gene I as a sensor of Hantaan virus replication. The Journal of General Virology 92:2191–2200.

Li X, Mooney P, Zheng S, Booth CR, Braunfeld MB, Gubbens S, Agard DA, Cheng Y. 2013. Electron counting and beam-induced motion correction enable near-atomic-resolution single-particle cryo-EM. Nature methods 10, 584-590.

Lin SC, Lo YC, Wu H. 2010. Helical assembly in the MyD88-IRAK4-IRAK2 complex in TLR/IL-1R signalling. Nature 465:885–890.

Liu S, Chen J, Cai X, Wu J, Chen X, Wu YT, Sun L, Chen ZJ. 2013. MAVS recruits multiple ubiquitin E3 ligases to activate antiviral signaling cascades. eLife 2:e00785.

Loo YM, Fornek J, Crochet N, Bajwa G, Perwitasari O, Martinez-Sobrido L, Akira S, Gill MA, Garcia-Sastre A, Katze MG, Gale M Jnr. 2008. Distinct RIG-I and MDA5 signaling by RNA viruses in innate immunity. Journal of Virology 82:335–345.

Loo YM, Gale M Jr. 2011. Immune signaling by RIG-I-like receptors. Immunity 34, 680-692.

Lu A, Magupalli VG, Ruan J, Yin Q, Atianand MK., Vos MR, Schroder GF, Fitzgerald K A, Wu H, Egelman EH. 2014. Unified polymerization mechanism for the assembly of ASC-dependent inflammasomes. Cell 156, 1193-1206.

Lu P, Bai XC, Ma D, Xie T, Yan C, Sun L, Yang G, Zhao Y, Zhou R, Scheres SH, Shi Y. 2014. Three-dimensional structure of human gamma-secretase. Nature 512, 166-170.

Ludtke SJ, Baldwin PR, Chiu W. 1999. EMAN: semiautomated software for high-resolution single-particle reconstructions. Journal of Structural Biology 128:82–97.

Luo D, Ding SC, Vela A, Kohlway A, Lindenbach BD, Pyle AM. 2011. Structural insights into RNA recognition by RIG-I. Cell 147:409–422.

Luo D, Kohlway A, Vela A, Pyle AM. 2012. Visualizing the determinants of viral RNA recognition by innate immune sensor RIG-I. Structure 20:1983–1988.

Luo D, Kohlway A, Pyle AM. 2013. Duplex RNA activated ATPases (DRAs): platforms for RNA sensing, signaling and processing. RNA Biology 10:111–120.

Malathi K, Dong B, Gale M, Silverman RH. 2007. Small self-RNA generated by RNase L amplifies antiviral innate immunity. Nature 448:816–19 38.

Malathi K, Saito T, Crochet N, Barton DJ, Gale M Jr, Silverman RH. 2010. RNase L releases a small RNA from HCV RNA that refolds into a potent PAMP. RNA 16:2108–19.

Marq JB, Hausmann S, Veillard N, Kolakofsky D, Garcin D. 2011. Short double-stranded RNAs with an overhanging 5’ ppp-nucleotide, as found in arenavirus genomes, act as RIG-I decoys. The Journal of Biological Chemistry 286:6108–6116.

McCoy AJ, Grosse-Kunstleve RW, Adams PD, Winn MD, Storoni LC, Read RJ. 2007. Phaser crystallographic software. Journal of Applied Crystallography 40:658–674.

Meylan E, Curran J, Hofmann K, Moradpour D, Binder M, Bartenschlager R, Tschopp J. 2005. Cardif is an adaptor protein in the RIG-I antiviral pathway and is targeted by hepatitis C virus. Nature 437:1167–1172.

Michelitsch MD, Weissman JS. 2000. A census of glutamine/asparagine-rich regions: implications for their conserved function and the prediction of novel prions. Proceedings of the National Academy of Sciences of the United States of America 97:11910–11915.

Mindell JA, Grigorieff N. 2003. Accurate determination of local defocus and specimen tilt in electron microscopy. J Struct Biol 142:334–47.

Mogensen TH. 2009. Pathogen recognition and inflammatory signaling in innate immune defenses. Clinical microbiology reviews 22, 240-273.

Mukherjee S, Zheng H, Derebe MG, Callenberg KM, Partch CL, Rollins D, Propheter

DC, Rizo J, Grabe M, Jiang QX, Hooper LV. 2014. Antibacterial membrane attack by a pore-forming intestinal C-type lectin. Nature 505:103–107.

Murali A, Li X, Ranjith-Kumar CT, Bhardwaj K, Holzenburg A, Li P, Kao CC. 2008. Structure and function of LGP2, a DEX(D/H) helicase that regulates the innate immunity response. The Journal of Biological Chemistry 283:15825–15833.

Myong S, Cui S, Cornish PV, Kirchhofer A,Gack MU, Jung JU, Hopfner K-P, Ha T. 2009. Cytosolic viral sensor RIG-I is a 5'-triphosphate- dependent translocase on double-stranded RNA. Science 323: 1070–1074.

Napetschnig J, Wu H. 2013. Molecular basis of NF-kappaB signaling. Annual Review of Biophysics 42:443–468.

Nelson R, Sawaya MR, Balbirnie M, Madsen AO, Riekel C, Grothe R, Eisenberg D. 2005. Structure of the cross-beta spine of amyloid-like fibrils. Nature 435:773–778.

Ni CZ, Welsh K, Leo E, Chiou CK, Wu H, Reed JC, Ely KR. 2000. Molecular basis for CD40 signaling mediated by TRAF3. Proceedings of the National Academy of Sciences of the United States of America 97:10395–10399.

Onoguchi K, Onomoto K, Takamatsu S, Jogi M, Takemura A, Morimoto S, Julkunen I, Namiki H, Yoneyama M, Fujita T. 2010. Virus-infection or 5'ppp-RNA activates antiviral signal through redistribution of IPS-1 mediated by MFN1. PLoS Pathogens 6:e1001012.

Orlova A, Garner EC, Galkin VE., Heuser J, Mullins RD, Egelman EH. 2007. The structure of bacterial ParM filaments. Nature structural & molecular biology *14*, 921-926.

Otwinowski Z, Minor W. 1997. Processing of X-ray diffraction data collected in oscillation mode. Methods in Enzymology 276:307–326.

Park YC, Burkitt V, Villa AR, Tong L, Wu H. 1999. Structural basis for self-association and receptor recognition of human TRAF2. Nature 398:533–538.

Patel JR, Jain A, Chou YY, Baum A, Ha T, Garcia-Sastre A. 2013. ATPase-driven oligomerization of RIG-I on RNA allows optimal activation of type-I interferon. EMBO Reports 14:780–787.

Peisley A, Lin C, Wu B, Orme-Johnson M, Liu M, Walz T, Hur S. 2011. Cooperative assembly and dynamic disassembly of MDA5 filaments for viral dsRNA recognition. Proceedings of the National Academy of Sciences of the United States of America 108:21010–21015.

Peisley A, Wu B, Yao H, Walz T, Hur S. 2013. RIG-I forms signaling-competent filaments in an ATP-dependent, ubiquitin-independent manner. Molecular Cell 51:573–583.

Peisley A, Wu B, Xu H, Chen ZJ, Hur S. 2014. Structural basis for ubiquitin-mediated antiviral signal activation by RIG-I. Nature 509, 110-114.

Pettersen EF, Goddard TD, Huang CC, Couch GS, Greenblatt DM, Meng EC, Ferrin TE. 2004. UCSF Chimera–a visualization system for exploratory research and analysis. Journal of Computational Chemistry 25:1605–1612.

Pickart CM, Raasi S. 2005. Controlled synthesis of polyubiquitin chains. Methods Enzymol 399, 21-36.

Potter JA, Randall RE, Taylor GL. 2008. Crystal structure of human IPS-1/MAVS/VISA/Cardif caspase activation recruitment domain. BMC Structural Biology 8:11.

Ranjith-Kumar CT, Murali A, Dong W, Srisathiyanarayanan D, Vaughan R, Ortiz-Alacantara J, Bhardwaj K, Li X, Li P, Kao CC. 2009. Agonist and antagonist recognition by RIG-I, a cytoplasmic innate immunity receptor. The Journal of Biological Chemistry 284:1155–1165.

Reikine S, Nguyen JB, Modis Y. 2014. Pattern Recognition and Signaling Mechanisms of RIG-I and MDA5. Frontiers in immunology 5, 342.

Ronald PC, Beutler B. 2010. Plant and animal sensors of conserved microbial signatures. Science 330:1061–1064.

Satoh T, Kato H, Kumagai Y, Yoneyama M, Sato S, Matsushita K, Tsujimura T, Fujita T, Akira S, Takeuchi O. 2010. LGP2 is a positive regulator of RIG-I- and MDA5-mediated antiviral responses. Proceedings of the National Academy of Sciences of the United States of America 107, 1512-1517.

Scheres SH. 2012. RELION: implementation of a Bayesian approach to cryo-EM structure determination. J. Struct. Biol. 180, 519–530.

Scheres SH. 2014. Beam-induced motion correction for sub-megadalton cryo-EM particles. eLife 3, e03665.

Schlee M, Roth A, Hornung V, Hagmann CA, Wimmenauer V, Barchet W, Coch C, Janke M, Mihailovic A, Wardle G, Juranek S, Kato H, Kawai T, Poeck H, Fitzgerald KA, Takeuchi O, Akira S, Tuschl T, Latz E, Ludwig J, Hartmann G. 2009. Recognition of 5’ triphosphate by RIG-I helicase requires short blunt double-stranded RNA as contained in

panhandle of negative-strand virus. Immunity 31:25–34.

Schlee M, Hartmann G. 2010. The chase for the RIG-I ligand--recent advances. Molecular therapy : the journal of the American Society of Gene Therapy *18*, 1254-1262.

Seth RB, Sun L, Ea CK, Chen ZJ. 2005. Identification and characterization of MAVS, a mitochondrial antiviral signaling protein that activates NF-kappaB and IRF3. Cell 122:669–682.

Strahle L, Marq JB, Brini A, Hausmann S, Kolakofsky D, Garcin D. 2007. Activation of the b interferon promoter by unnatural Sendai virus infection requires RIG-I and is inhibited by viral C proteins. J Virol 81: 12227–12237.

Takeuchi O, Akira S. 2010. Pattern recognition receptors and inflammation. Cell 140:805–820. Venkataraman T, Valdes M, Elsby R, Kakuta S, Caceres G, et al. 2007. Loss of DExD/H box RNA helicase LGP2 manifests disparate antiviral responses. J. Immunol. 178:6444–55.

Wang YA, Yu X, Yip C, Strynadka NC, Egelman EH. 2006. Structural polymorphism in bacterial EspA filaments revealed by Cryo-EM and an improved approach to helical reconstruction. Structure 14:1189-1196.

Wriggers W. 2010. Using Situs for the integration of multi-resolution structures. Biophysical Reviews 2:21–27.

Wu B, Peisley A, Richards C, Yao H, Zeng X, Lin C, Chu F, Walz T, Hur S. 2013. Structural basis for dsRNA recognition, filament formation, and antiviral signal activation by MDA5. Cell 152:276–289.

Wu B, Peisley A, Tetrault D, Li Z, Egelman EH, Magor KE, Walz T, Penczek PA, Hur S. 2014. Molecular imprinting as a signal-activation mechanism of the viral RNA sensor RIG-I. Molecular cell 55, 511-523.

Wu J, Chen ZJ. 2014. Innate immune sensing and signaling of cytosolic nucleic acids. Annual review of immunology 32, 461-488.

Xu H, He X, Zheng H, Huang LJ, Hou F, Yu Z, de la Cruz MJ, Borkowski B, Zhang X, Chen ZJ, Jiang QX. 2014. Structural basis for the prion-like MAVS filaments in antiviral innate immunity. eLife *3*, e01489.

Xu LG, Wang YY, Han KJ, Li LY, Zhai Z, Shu HB. 2005. VISA is an adapter protein required for virus-triggered IFN-beta signaling. Molecular Cell 19:727–740.

Yasukawa K, Oshiumi H, Takeda M, Ishihara N, Yanagi Y, Seya T, Kawabata S,

Koshiba T. 2009. Mitofusin 2 inhibits mitochondrial antiviral signaling. Science signaling 2:ra47.

Yoneyama M, Kikuchi M, Matsumoto K, Imaizumi T, Miyagishi M, Taira K, Foy E, Loo YM, Gale M Jr, Akira S, et al. 2005. Shared and unique functions of the DExD/H-box helicases RIG-I, MDA5, and LGP2 in antiviral innate immunity. J Immunol 175, 2851-2858.

Yoneyama M, Fujita T. 2009. RNA recognition and signal transduction by RIG-I-like receptors. Immunological Review 227:54–65.

Yoneyama M, Kikuchi M, Natsukawa T, Shinobu N, Imaizumi T, Miyagishi M, Taira K, Akira S, Fujita T. 2004. The RNA helicase RIG-I has an essential function in double-stranded RNA-induced innate antiviral responses. Nature Immunology 5:730–737.

Yu Z, Dobro MJ, Woodward CL, Levandovsky A, Danielson CM, Sandrin V, Shi J, Aiken C, Zandi R, Hope TJ, Jensen GJ. 2013. Unclosed HIV-1 capsids suggest a curled sheet model of assembly. Journal of Molecular Biology 425:112–123.

Zeng W, Sun L, Jiang X, Chen X, Hou F, Adhikari A, Xu M, Chen ZJ. 2010. Reconstitution of the RIG-I pathway reveals a signaling role of unanchored polyubiquitin chains in innate immunity. Cell 141:315–330.

Zheng C, Kabaleeswaran V, Wang Y, Cheng G, Wu H. 2010. Crystal structures of the TRAF2: cIAP2 and the TRAF1: TRAF2: cIAP2 complexes: affinity, specificity, and regulation. Molecular Cell 38:101–113.